



**HAL**  
open science

# Multiscale modeling of the elasto-plastic behavior of architected and nanostructured Cu-Nb composite wires and comparison with neutron diffraction experiments

Tang Gu, J. R. Medy, Vincent Klosek, Olivier Castelnau, Samuel Forest, Eveline Hervé-Luanco, F. Lecouturier-Dupouy, Henry Proudhon, Pierre Olivier Renault, Ludovic Thilly, et al.

## ► To cite this version:

Tang Gu, J. R. Medy, Vincent Klosek, Olivier Castelnau, Samuel Forest, et al.. Multiscale modeling of the elasto-plastic behavior of architected and nanostructured Cu-Nb composite wires and comparison with neutron diffraction experiments. *International Journal of Plasticity*, 2019, 122, pp.1-30. 10.1016/j.ijplas.2019.04.011 . hal-02266595v2

**HAL Id: hal-02266595**

**<https://hal.science/hal-02266595v2>**

Submitted on 28 Jan 2020

**HAL** is a multi-disciplinary open access archive for the deposit and dissemination of scientific research documents, whether they are published or not. The documents may come from teaching and research institutions in France or abroad, or from public or private research centers.

L'archive ouverte pluridisciplinaire **HAL**, est destinée au dépôt et à la diffusion de documents scientifiques de niveau recherche, publiés ou non, émanant des établissements d'enseignement et de recherche français ou étrangers, des laboratoires publics ou privés.

# Multiscale modeling of the elasto-plastic behavior of architected and nanostructured Cu-Nb composite wires and comparison with neutron diffraction experiments

T. Gu<sup>a,b</sup>, J.-R. Medy<sup>e</sup>, V. Klosek<sup>f</sup>, O. Castelnaud<sup>a</sup>, S. Forest<sup>b,\*</sup>, E. Hervé-Luanco<sup>c,b</sup>, F. Lecouturier–Dupouy<sup>d</sup>, H. Proudhon<sup>b</sup>, P.-O. Renault<sup>e</sup>, L. Thilly<sup>e</sup>, P. Villechaise<sup>e</sup>

<sup>a</sup> PIMM, CNRS UMR 8006, Arts et Métiers ParisTech, CNAM, 151 Bd de l'Hôpital, 75013 Paris, France

<sup>b</sup> MINES ParisTech, PSL Research University, MAT-Centre des matériaux, CNRS UMR 7633, BP 87, 91003 Evry, France

<sup>c</sup> Université de Versailles, Saint-Quentin en Yvelines, 45 Avenue des Etats-Unis, 78035 Versailles Cedex, France

<sup>d</sup> Laboratoire National des Champs Magnétiques Intenses, EMFL, UPR 3228 CNRS-INSA-UGA-UPS, Grenoble & Toulouse, France

<sup>e</sup> Institut Pprime, UPR 3346, CNRS, University of Poitiers, ISAE-ENSMA, SP2MI, Boulevard Marie et Pierre Curie, BP 30179, 86692 Futuroscope Chasseneuil Cedex, France

<sup>f</sup> Laboratoire Léon Brillouin, CEA-Saclay, 91191 Gif-sur-Yvette Cedex, France

## ARTICLE INFO

### Keywords:

Multiscale modeling  
Copper niobium wire  
Elasto-plasticity  
Homogenization  
Polycrystalline material  
Neutron diffraction

## ABSTRACT

Nanostructured and architected copper niobium composite wires are excellent candidates for the generation of intense pulsed magnetic fields ( $\sim 100\text{T}$ ) as they combine both high strength and high electrical conductivity. Multi-scaled Cu-Nb wires are fabricated by accumulative drawing and bundling (a severe plastic deformation technique), leading to a multiscale, architected, and nanostructured microstructure exhibiting a strong fiber crystallographic texture and elongated grain shape along the wire axis. This paper presents a comprehensive study of the effective elasto-plastic behavior of this composite material by using two different approaches to model the microstructural features: full-field finite elements and mean-field modeling. As the material exhibits several characteristic scales, an original hierarchical strategy is proposed based on iterative scale transition steps from the nanometric grain scale to the millimetric macro-scale. The best modeling strategy is selected to estimate reliably the effective elasto-plastic behavior of Cu-Nb wires with minimum computational time. Finally, for the first time, the models are confronted to tensile tests and in-situ neutron diffraction experimental data with a good agreement.

## 1. Introduction

In recent years, two types of filamentary and multilayered nano-composites composed of copper and niobium (i.e. Cu-Nb nano-composite wires and laminates) have been highlighted thanks to their special properties (Misra and Thilly, 2010). These two Cu-Nb nano-composites are fabricated respectively by two different severe plastic deformation techniques: Accumulative Drawing and Bundling (Dupouy et al., 1996; Thilly, 2000; Vidal, 2006; Dubois, 2010; Medy, 2016) and Accumulated Roll Bonding (Lim and Rollett, 2009; Beyerlein et al., 2014).

A typical cross section of a Cu-Nb nano-composite wire is illustrated in Fig. 1, referred to as “Filamentary” structure in Thilly (2000); Thilly et al. (2002): a multiscale Cu matrix embedding parallel Nb nano-filaments. These nano-composite conductors are

\* Corresponding author.

E-mail address: samuel.forest@mines-paristech.fr (S. Forest).

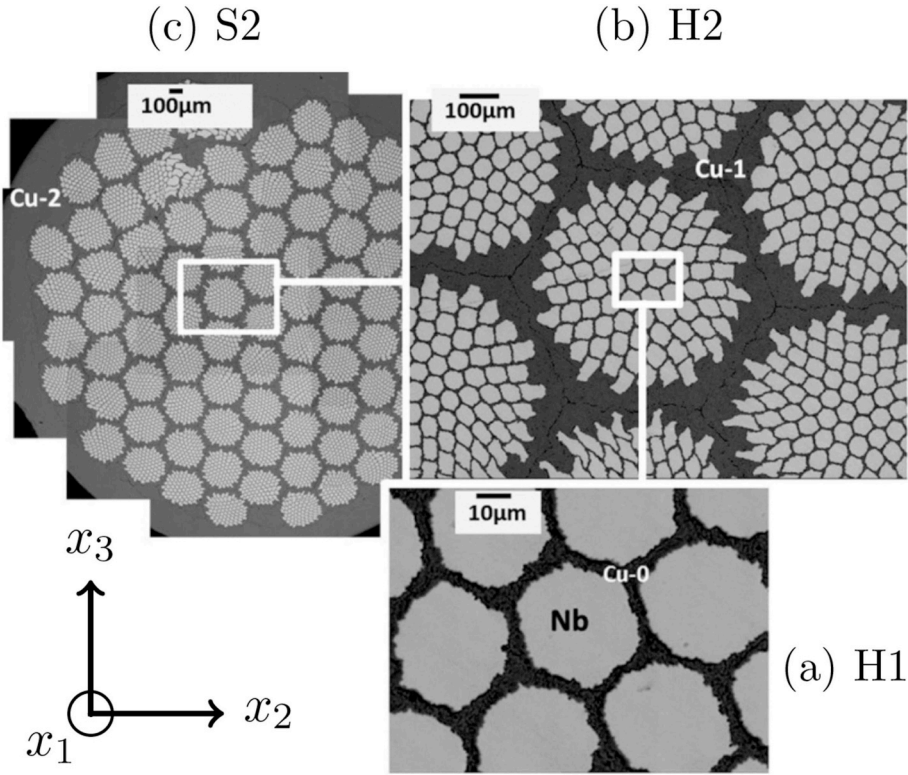


**Fig. 1.** Successive section views of the Cu-Nb nano-composite wires containing  $85^2$  elementary Cu/Nb long fibers. The diameter of specimen (c) is reduced from actual 4.50 mm to two smaller diameters by supplementary cold-drawing: 2.10 mm for in-situ neutron diffraction experiments and 0.29 mm for macroscopic tensile tests in this work. The smaller scale for pure polycrystalline Cu or Nb (i.e. scale H0) is not shown in this figure. See Section 2.3 for scale conventions and notations.

excellent candidates for generation of intense pulsed magnetic fields ( $\sim 100T$ ). The intense magnetic field offers valuable opportunity to carry out many of the essential experiments (e.g. in the field of particle physics), and become promising industrial tools (such as controlled nuclear fusion) (Spencer et al., 2004; Jaime et al., 2012; Béard et al., 2013, 2018; Halperin et al., 2013; Debray and Frings, 2013; Zherlitsyn et al., 2013; Frydman, 2014; Peng et al., 2014; Nguyen et al., 2016). To generate them, the conductors for the winding coils must combine both high mechanical strength (due to large Lorentz forces) and high electrical conductivity. In Thilly (2000); Vidal et al. (2007), a conductor presenting an ultimate tensile strength as large as 1.9 GPa at 77 K has been obtained, together with an electrical conductivity of  $1.72 \mu\Omega^{-1} \text{cm}^{-1}$ .

Predicting the elasto-plastic behavior of polycrystalline nano-composites with respect to their nano/micro-structure is a complex matter, particularly if they are fabricated by severe plastic deformations leading to:

- (1) specific crystallographic/morphological textures;
- (2) microstructural features which exhibit anisotropy and induce size effects;
- (3) initial residual stresses.

In this field, combining material characterization and multiscale modeling is mandatory. Previous studies on the Cu-Nb nano-composite wires and laminates have focused on textures and their evolution (Lim and Rollett, 2009; Dubois, 2010; Lee et al., 2012; Hansen et al., 2013; Medy, 2016), elasticity (Gu et al., 2017a), dislocation glide (Thilly et al., 2001; Misra and Hoagland, 2007), grain size dependent yield stress/yield criterion (Misra and Hoagland, 2007; Thilly et al., 2009; Nizolek et al., 2015), Bauschinger effect (Thilly et al., 2007; Badinier et al., 2014), hardness (Thilly et al., 2002), ultimate tensile strength (Vidal et al., 2007), Cu-Nb interfaces (Mayeur et al., 2013, 2015; Beyerlein et al., 2014), and thermal stability and internal stresses (Vidal, 2006; Dubois et al., 2010; Beyerlein et al., 2014). The electrical behavior of Cu-Nb composites was studied by Gu et al. (2015, 2017b).

The present work concentrates on the multiscale modeling of the *anisotropic elasto-plastic behavior* of architected and nano-structured Cu-Nb composite *wires*. Two multi-scale methods will be introduced: a full-field Finite Element Method (FEM, see Table 1 for the abbreviations) with periodic boundary conditions (denoted PH, for Periodic Homogenization) and a mean-field homogenization model, i.e. the so-called “ $\beta$ -models” after Caillaud (1992); Pilvin (1996). These models essentially differ by the microstructural information they are based on for the estimation of effective behavior. Here, FEM PH assumes a periodic microstructure adapted for polycrystalline aggregates and for hexagonal fiber assemblies (present at different scales in Fig. 1). On the other hand,  $\beta$ -

**Table 1**

The abbreviations used in this work.

FEM	Finite Element Method	PH	Periodic Homogenization
SSC	Standard Self-Consistent scheme	RVE	Representative Volume Element
OFHC Cu	Oxygen-Free High Conductivity Cu	CRSS	Critical Resolved Shear Stress
LT	Longitudinal Tensile test	TT	Transverse Tensile test
TS	Transverse Shear test	LS	Longitudinal Shear test

models will be used to describe the elasto-plastic behavior of polycrystals made of Cu or Nb grains, but also for the estimation of a random mixture of Cu and Nb phases. The results provided by FEM are also regarded as benchmarks to identify parameters of the  $\beta$ -model.

Taking into account dislocation movements for strain hardening of a single crystal, dislocation-based constitutive formulations have been proposed in the literature, e.g. [Asaro \(1983\)](#); [Tabourot et al. \(1997\)](#); [Hoc and Forest \(2001\)](#); [Kubin et al. \(2008\)](#); [Devincre et al. \(2008\)](#); [Groh et al. \(2009\)](#) for BCC (Body-Centered Cubic) and FCC (Face-Centered Cubic) crystals. In these models, all parameters have a physical meaning which can be determined by experiments or other theoretical analysis, such as dislocation dynamics ([Tabourot et al., 1997](#); [Groh et al., 2009](#)). The Méric-Cailletaud's model is more phenomenological in nature and uses an original combination of kinematic and isotropic hardening for each slip system ([Méric et al., 1991](#); [Besson et al., 2009](#)). This model was used for the crystal plastic predictions of metallic alloys, particularly for FCC Cu polycrystals ([Méric et al., 1994](#); [Šiška et al., 2006](#); [Musienko et al., 2007](#); [Gérard, 2008](#); [Šiška et al., 2009](#)). Here, the Méric-Cailletaud model will be used to describe the visco-plastic constitutive law for single Cu crystals.

Full-field methods (e.g. based on FEM) applied to a Representative Volume Element (RVE) can integrate the detailed experimental microstructure and provide the complex stress/strain fields inside the different phases. The elasto-(visco-)plastic effective behavior of FCC and BCC polycrystalline aggregates can be studied by FEM in many aspects, as shown in [Barbe et al. \(2001a, b\)](#); [Fritzen and Böhlke \(2011\)](#). In addition, in order to save computational time, another full-field method, using Fast Fourier Transform (FFT) to solve the mechanical equilibrium, has been developed for both linear and nonlinear polycrystalline behavior ([Moulinec and Suquet, 1995](#); [Suquet et al., 2012](#); [Lebensohn et al., 2012](#)). Furthermore, for heterogeneous materials with a random or complex microstructure, e.g. the hexagonal fiber assembly, the elasto-(visco-)plastic scale transition is a challenge for homogenization models. In this regard, the following attempts are worth mentioning: the above-mentioned full-field FEM ([Williams and Pindera, 1997](#)), macroscopic model with phenomenological parameters identified from field measurements ([Haddadi et al., 2006](#)),  $FE^2$  multiscale approach ([Feyel and Chaboche, 2000](#); [Geers et al., 2010](#)), and TFA (Transformation Field Analysis)/NTFA (Nonuniform Transformation Field Analysis) ([Michel and Suquet, 2003, 2004, 2016](#); [Franciosi and Berbenni, 2008](#); [Fritzen and Böhlke, 2011](#)). The latter method represents a transition from full field to mean field models.

The mean-field method relying on homogenization theory is well adapted to estimate the mechanical behavior of polycrystals. Unlike full-field approaches, the mean-field method is based on a statistical description of the microstructure of polycrystalline aggregates leading to reduced computational time. These methods were initially developed for heterogeneous linear thermal-elasticity, such as the Standard Self-Consistent scheme (denoted SSC), see the original references quoted in [François et al. \(1998\)](#); [Qu and Cherkaoui \(2006\)](#); [Nemat-Nasser and Hori \(2013\)](#). Later on, they have been extended to (i) visco-plastic, (ii) elasto-plastic and (iii) elasto-visco-plastic nonlinear properties ([Ponte-Castañeda and Suquet, 1998](#)). For nonlinear homogenization, the main difficulty relies on a carefully chosen linearization for the material properties. Use is made of a “linear comparison material” which exhibits a thermo-elastic like behavior defined at each strain value or increment. For (i) visco-plastic materials, one can perform a secant linearization ([Hutchinson, 1976](#)), a tangent one ([Molinari et al., 1987](#); [Lebensohn and Tomé, 1994](#)) and an affine one ([Masson and Zaoui, 1999](#)). These approaches have been improved by using stress/strain heterogeneities inside the phases leading to so-called second-order moments ([Castañeda, 1991, 2002](#)). For (ii) elasto-plastic materials, [Kröner \(1978\)](#) proposed an incremental approach in which the interaction between the grain and the effective medium is purely elastic. This leads to an overestimation of the effective stress ([Berveiller and Zaoui, 1978](#); [Masson and Zaoui, 1999](#)). In order to (at least partly) figure out this issue, many later works, e.g. [Berveiller and Zaoui \(1978\)](#); [Turner and Tomé \(1994\)](#); [Masson et al. \(2000\)](#); [Neil et al. \(2010\)](#); [Doghri et al. \(2011\)](#); [Wu et al. \(2013\)](#); [Zecevic and Knezevic \(2015\)](#) have considered an elasto-plastic interaction law instead of an elastic one. Based on the [Berveiller and Zaoui \(1978\)](#) model for isotropic nonlinear behavior of equiaxed polycrystals, the  $\beta$ -models were proposed for anisotropic behavior of multi-axial polycrystals ([Cailletaud, 1992](#); [Forest and Pilvin, 1996](#); [Sai et al., 2006](#); [Martin et al., 2014](#); [Cailletaud and Coudon, 2016](#); [Coudon, 2017](#); [Coudon et al., 2018](#)). For (iii) elasto-visco-plastic behavior, one specific difficulty is the “long term memory effect” leading to a time delay of the interphase mechanical interactions. Different solutions have also been proposed, such as [Masson and Zaoui \(1999\)](#); [Paquin et al. \(1999, 2001\)](#); [Brenner et al. \(2002\)](#); [Vu et al. \(2012\)](#).

Despite a wealth of literature works on elasto-(visco-)plasticity of crystals, we have found that the following three points are still missing:

- (1) A systematic analysis of the anisotropic behavior for Cu/Nb polycrystals by elasto-plastic homogenization models, especially for the specific crystallographic/morphological textures encountered in Cu-Nb wires;
- (2) An iterative scale transition homogenization approach accounting for elasto-plasticity adapted for the recent Cu-Nb wires with a complex architecture (i.e. the multi-scaled hexagonal fiber assemblies), and including the effect of initial residual stresses;
- (3) An interpretation of recent experimental mechanical test data of Cu-Nb wires, particularly the in-situ neutron diffraction data in

Medy (2016). It should be noted that only tensile tests can be performed in-situ with such thin wires.

Therefore, the objectives of the present work are threefold:

- (1) Provide a homogenization model for individual Cu and Nb polycrystals present in the composite wires taking into account the crystallographic and morphological textures;
- (2) Provide a multi-scale homogenization procedure to model the architected and nanostructured Cu-Nb composite wires, accounting for initial residual stresses and grain size effects;
- (3) Provide a quantitative understanding of the load dependency of crystal lattice evolution during neutron diffraction uniaxial loading test for Cu-Nb wires.

Accordingly, the outline of the article is as follows. The architecture/microstructure of Cu-Nb wires and the induced mechanical properties are described in Section 2. In order to reproduce the effective elasto-plastic behavior of this material, two multi-scale methods, i.e. full-field periodic models and the  $\beta$ -models are presented in Section 3. In Section 4, the elasto-plastic Cu polycrystals are isolated and homogenized. Then in Section 5, several scale transitions of architected Cu-Nb composites are performed to determine the effective elasto-plastic behavior of Cu-Nb wires up to macro-scale. The uncertainties of scale transition are discussed and the best-suited modeling strategy is selected. Finally, in Section 6, the model results are validated by comparison with macroscopic mechanical data from tensile tests and lattice strains from neutron diffraction.

Throughout this work, the following notation is used:  $x$  for scalars,  $\underline{x}$  for vectors,  $\underline{\underline{x}}$  for 2nd-order tensors,  $\underline{\underline{\underline{x}}}$  for 4th-order tensors,  $\cdot$  for single contraction,  $:$  for double contraction,  $\otimes$  for tensor product,  $\bar{x}$  for effective (or homogenized) property and  $\bar{x} = \langle x \rangle$  for volume average.

## 2. Material description

### 2.1. Fabrication process

Cu-Nb nano-composite wires are fabricated via a severe plastic deformation process, based on ADB (series of hot extrusion, cold drawing and bundling stages) according to (Dupouy et al., 1996; Thilly, 2000; Vidal, 2006; Dubois, 2010; Medy, 2016):

- A Nb wire is initially inserted into a Cu tube. The used Cu is Oxygen-Free High Conductivity (OFHC).
- The structure is extruded and drawn, then cut into 85 smaller pieces with hexagonal cross section.
- These pieces are then bundled and inserted into a new Cu tube.
- The new composite structure is again extruded and drawn. And so on.

In the present work, ADB is repeated twice, leading to copper based architected and nanostructured composite wires which are composed of a multi-scale Cu matrix embedding  $85^2$  Nb nanofibers (so-called  $N = 85^2$  type of “Cu-Nb Filamentary” wires, as illustrated in Fig. 1): Nb fibers are separated by the finest Cu-0 copper channels; groups of 85 Nb/Cu-0 elementary long fibers are then separated by Cu-1 copper channels; the group of  $85^2$  elementary patterns is finally embedded in an external Cu-2 copper jacket. It is noted that, unlike Cu, Nb fibers are introduced only at the very first fabrication stage. Therefore, Nb fibers are all deformed together during the iterative ADB process, and should exhibit the same microstructure with similar characteristic sizes. In contrast, copper is introduced at each stage so that several types of copper microstructures are present in the material. The Cu-0 regions originate from the beginning of the process, while the Cu-1 and Cu-2 are introduced successively during the two steps of ADB; different microstructures are thus expected for the different Cu- $i$  regions ( $i = 0, 1, \text{ and } 2$ ).

In this work, two Cu-Nb Filamentary wires with a final diameter<sup>1</sup> of 0.29 mm and 2.10 mm are used for macroscopic tensile testing and in-situ neutron diffraction experiments. These wires are obtained from initial specimens with a diameter of 4.50 mm by supplementary cold-drawings (Medy, 2016). The volume fractions  $f$  of each component (i.e. Nb, Cu-0, Cu-1 and Cu-2) are not altered by hot-extrusion nor cold-drawing and they can be determined from the initial dimensions of Nb cylinder and Cu jacket. The theoretical value of channel width,  $\delta$ , can be estimated assuming a homogeneous deformation of the structure during the material processing (Vidal, 2006), as indicated in Table 2 for the two diameters.

### 2.2. Crystallographic and morphological textures

The study of the elastic behavior of the wires performed by (Gu et al., 2017a) shows that the effective wire behavior critically depends on the grain morphology and texture. In particular, accounting for the crystallographic textures is of the utmost importance and will be part of the proposed multiscale modeling of elasto-plasticity in this work. The crystallographic texture of the Cu-Nb Filamentary wire of interest at a diameter of 4.50 mm has been investigated by EBSD at various scales by Medy (2016). Fig. 2 illustrates the EBSD orientation map of a the cross section perpendicular to the wire axis  $x_1$  at the effective scale H1. The Cu grains

<sup>1</sup> Following (Thilly et al., 2002; Medy, 2016), all dimensions are given in the  $x_2x_3$  cross section, i.e. perpendicular to the wire axis  $x_1$ , see Fig. 1 for the coordinate system.

**Table 2**

Volume fraction  $f$ , channel width  $\delta$ , crystallographic textures and yield stresses  $\sigma_y$  of individual component for Cu and Nb polycrystals in Cu-Nb wires, obtained experimentally in Medy (2016). The two wires with different diameters are assumed to exhibit similar crystallographic textures. Yield stresses  $\sigma_y$  are  $>2$  GPa for Nb,  $\sim 350$  MPa for Cu-1 and Cu-2, and 500MPa for Cu-0 with channel width  $\delta = 310$  nm.

Component	Nb	Cu-0	Cu-1	Cu-2
Volume fraction $f$	44.7%	15.2%	17.5%	22.6%
Channel width $\delta$				
wire diameter: 2.10 mm	13.74 $\mu\text{m}$	2.19 $\mu\text{m}$	21.97 $\mu\text{m}$	124.48 $\mu\text{m}$
wire diameter: 0.29 mm	1.94 $\mu\text{m}$	310 nm	3.09 $\mu\text{m}$	17.65 $\mu\text{m}$
Fiber textures				
$\langle 111 \rangle$	–	70%	90%	81%
$\langle 100 \rangle$	–	30%	10%	19%
$\langle 110 \rangle$	100%	–	–	–

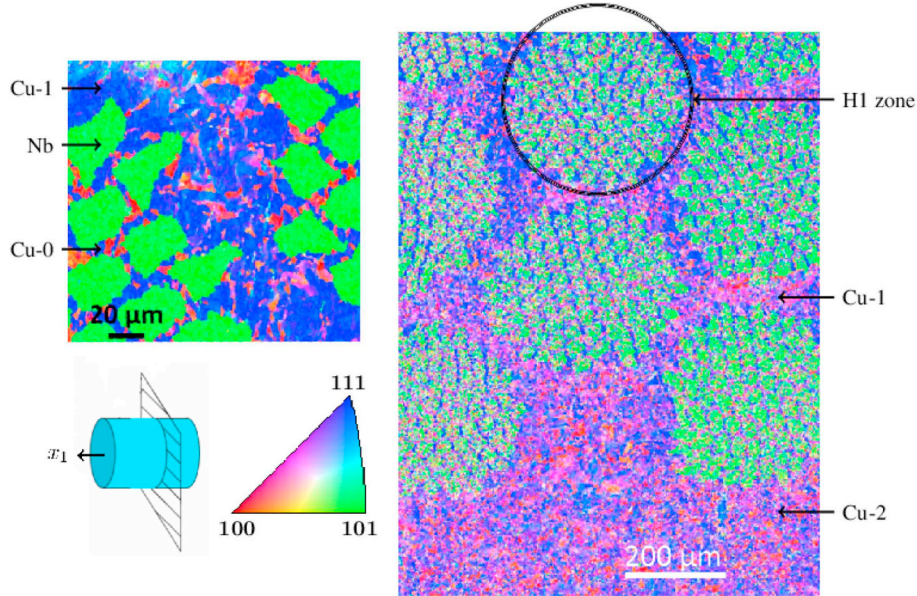


**Fig. 2.** EBSD map in the  $x_2 - x_3$  transverse plane showing Cu and Nb grain orientations (Medy, 2016). Inverse pole figure ( $x_1$  axis) coloring according to the cubic crystal system. Nb appears in green due to the strong  $\langle 110 \rangle$  fiber texture and Cu in red/blue. The specimen diameter is 4.50 mm. (For interpretation of the references to color in this figure legend, the reader is referred to the Web version of this article.)

exhibit a strong  $\langle 111 \rangle$  fiber texture with a remnant  $\langle 100 \rangle$  fiber, while a single  $\langle 110 \rangle$  texture is observed for Nb. Due to extrusions and drawings along the wire direction in the material processing,  $x_1$  is the symmetry axis of these fibers. The crystallographic textures of each component are given in Table 2. The associated texture spread (i.e. FWHM, for Full Width at Half Maximum) is estimated to be  $10.0^\circ \pm 3.0^\circ$ , based on EBSD data. The specimens with smaller diameters 2.10 and 0.29 mm studied in this work are assumed to display very similar crystallographic texture.

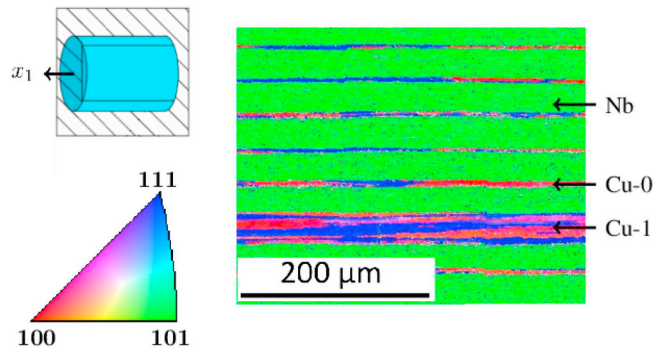


**Fig. 3.** EBSD map in a plane parallel to  $x_1$  showing Cu and Nb grain orientations (Medy, 2016). Inverse pole figure ( $x_1$  axis) coloring according to the cubic crystal system. The specimen diameter is 4.50 mm. Highly elongated grains along  $x_1$  are observed for all components (e.g. Cu-1 in this figure).

In the following,  $\ell$  is defined as the average grain length along the longitudinal wire axis  $x_1$  and  $d$  as the average grain diameter in the transverse  $x_2$ - $x_3$  cross section. As illustrated in Fig. 3 obtained by EBSD (Medy, 2016), the morphological texture exhibits highly elongated grains along  $x_1$  because of iterative severe plastic extrusion and drawing, i.e.  $\ell \gg d$  for both Cu and Nb components.

### 2.3. Scale conventions

For multiscale modeling of the effective elasto-plastic behavior of these Cu-Nb wires, the following scale conventions will be used (see Fig. 1):

- Scale H0. Homogenization at the highest magnification scale, looking directly at each individual polycrystalline Cu or Nb aggregate, is labeled as H0 (Homogenization 0). In other words, the effective stress-strain denoted  $(\bar{\sigma}-\bar{\epsilon})_{H0}$  at scale H0 of pure Cu (or pure Nb) polycrystalline aggregates will be obtained from the homogenization models.
- Scale H1. Homogenization at the scale of a bundle unit containing  $85^1$  elementary Nb/Cu-0 long fibers is labeled as H1 (Homogenization 1).
- Scale H2. Iterative homogenization at the scale where the effective Cu-Nb composite H1 zones are embedded in the Cu-1 matrix is labeled as H2 (Homogenization 2), i.e. H2 provides the effective behavior of an assembly of  $85^2$  elementary patterns. The effective behavior is labeled as  $(\bar{\sigma}-\bar{\epsilon})_{Hi}$  at scales Hi of the bundle unit of  $85^i$  ( $i = 1, 2$ ) elementary long fibers.
- Scale S2. The macroscopic scale S2 is defined here as a single cylinder-shaped Structure with two layers: effective Cu-Nb composite H2 core zone surrounded by the external Cu-2 jacket. The structural problem S2 will be solved by FEM to compute the macroscopic behavior  $(\bar{\sigma}-\bar{\epsilon})_{S2}$ . Then, this effective behavior will be compared with available experimental data.

In addition, the effective elastic stiffness tensors are noted as  $\left(\tilde{C}_{\approx}^i\right)_{Hi}$  and  $\left(\tilde{C}_{\approx}^i\right)_{S2}$  at scales Hi ( $i = 0,1,2$ ) and S2 respectively as in (Gu et al., 2017a). Finally, due to the combination of the axisymmetric morphological and crystallographic textures of Cu and Nb aggregates with the successive quasi-hexagonal arrangements of fibers or bundles, the effective behavior is expected to exhibit *transverse isotropy* with respect to  $x_1$  at all scales H0 to S2.

### 2.4. Grain size dependent yield stress

Different types of copper matrix channels are present (Thilly et al., 2009), due to the multi-scale microstructures: (1) Cu channels with  $\delta$  larger than a few micrometers (i.e. the so-called “large” Cu channels) which are composed of grains with a transverse size  $d \sim 1 \mu\text{m}$  together with remaining smaller grains with  $d = 200\text{--}400 \text{ nm}$  (a typical grain size in cold-worked Cu); (2) The “fine” Cu-0 channels lie in the sub-micrometer range, with only a few grains located between the Cu/Nb interfaces: in this case, the grain width  $d$  varies from  $\delta/3$  to  $\delta$ .

According to Vidal et al. (2007); Thilly et al. (2009), the yield stress  $\sigma_y$  of the highly cold worked large Cu channels can be estimated as 350 MPa. Furthermore, it was observed unambiguously that plastic deformation proceeds in the fine Cu-0 channels by emission of individual dislocation loops at one Cu-Nb interface, then gliding in the Cu-0 grain interior and absorption in the neighbouring Cu-Nb interface (Thilly et al., 2001). As a result, edge segments are absorbed in the Cu/Nb interfaces and screw segments bow out between two interfaces, eventually propagating by further bowing and deposition of dislocation debris at interfaces. Such a “single dislocation” regime is usually related to the Orowan-type behavior where the enhanced yield stress  $\sigma_y$  can be related to the channel width  $\delta$  as:  $\sigma_y = \sigma_y^0 + \alpha\mu(b/\delta)\ln(\delta/b)$  where  $\mu = 42.5 \text{ GPa}$ ,  $b_{Cu} = 0.256 \text{ nm}$  and  $\alpha = 0.6$  denotes respectively shear modulus, norm of Burgers vector and a material constant depending on the dislocation character together with the Taylor factor (Thilly et al., 2009). In addition,  $\sigma_y^0$  is 350 MPa corresponding to the yield stress of “coarse grain” in large Cu channels. By using this grain size effect formula, the finest Cu-0 channels with  $\delta = 310 \text{ nm}$  are expected to display a higher  $\sigma_y$  up to 500 MPa. In contrast, Cu-0 channels with  $\delta = 2.19 \mu\text{m}$  still display a  $\sigma_y$  of 350 MPa, when wire diameter takes 2.10 mm.

The bulk specimens of cold worked polycrystalline Nb display a  $\sigma_y \sim 1.4 \text{ GPa}$  (Dupouy et al., 1995). On the other hand, Nb grain size  $d_{Nb}$  is comparable with the fiber diameter (Thilly et al., 2009). Due to size effects, Dubois et al. (2012) argued that  $\sigma_y$  of Nb fibers is much higher ( $>2 \text{ GPa}$ ) than  $\sigma_y$  of Cu channels. Several ex-situ/in-situ tensile tests of Cu-Nb wires were performed along the wire direction  $x_1$  up to macroscopic material failure, and plastic strain has not been observed in the Nb fibers (Vidal, 2006; Dubois, 2010). Therefore, Nb is assumed to remain elastic for the small-strain mechanical tests considered in this work. All yield stress values  $\sigma_y$  of the various components considered in this work are summarized in the legend of Table 2.

### 2.5. Initial residual stresses

Due to the material processing, residual stresses, denoted by  $\sigma_{res}$ , are initially introduced in composite Cu-Nb wires, as observed by X-ray diffraction (Vidal, 2006). The longitudinal initial residual stresses  $(\sigma_{res})_{11}$  along the wire axis  $x_1$  have been determined in a Cu-Nb wire containing  $N = 55^4$  elementary Cu/Nb fibers (specimen diameter 1.49 mm): Axial compression  $\sim -100 \text{ MPa}$  for the large Cu channels ( $\delta \geq 1 \mu\text{m}$ ) and axial tension  $\sim +250 \text{ MPa}$  in the Nb phase. However,  $\sigma_{res}$  could not be determined accurately, and have not been reported for the Cu-Nb Filamentary wires  $N = 85^2$  studied in this work. The identification of  $\sigma_{res}$  will be discussed later in Section 6.2.

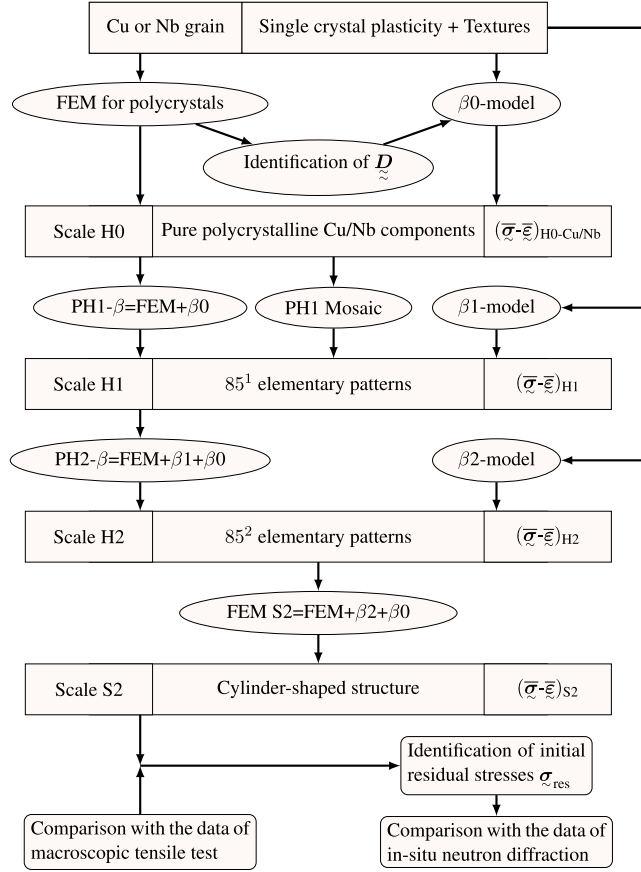


**Fig. 4.** Overview chart of the iterative scale transition steps and experimental comparison. The considered scales and scale transition models are mentioned, together with the obtained effective behavior. The identification of initial residual stresses is also shown. The same parameter combination of  $D_j$  is used for all the  $\beta_i$ -model ( $i = 0, 1, 2$ ), once identified at scale H0.

### 3. Hierarchical homogenization strategy

The homogenization strategy used in this work, including the corresponding scales, models used, results obtained and identification of initial residual stresses, is illustrated in Fig. 4.

#### 3.1. Constitutive equations for the single crystal

The Cu-Nb wires are made of FCC Cu and BCC Nb grains. Nb exhibits a high yield stress and therefore only the elastic behavior will be considered, i.e. no plastic strain assumed (Section 2.4). This section presents the elasto-visco-plastic single crystal model used for the Cu components. The Méric-Cailletaud model has been developed in the framework of crystal plasticity theory following (Méric et al., 1991) and used for several metallic alloys. It is presented here in its small perturbation version, which uses an additive decomposition of the total strain rate into elastic and viscoplastic parts.

The resolved shear stress  $\tau^s$  acting on a particular slip system ( $s$ ) is given by Schmid's law:

$$\tau^s = \boldsymbol{\sigma}^{(r)} : \mathbf{m}^s \quad (1)$$

where  $\boldsymbol{\sigma}^{(r)}$  is the stress tensor in a crystal phase ( $r$ ) and  $\mathbf{m}^s$  is the orientation tensor attributed to the slip system ( $s$ ):

$$\mathbf{m}^s = \frac{1}{2} (\mathbf{l}^s \otimes \mathbf{n}^s + \mathbf{n}^s \otimes \mathbf{l}^s) \quad (2)$$

with unit vectors  $\mathbf{n}^s$  and  $\mathbf{l}^s$  being the “slip plane” normal and the “slip direction”, respectively. Here, 12 octahedral systems are considered for FCC Cu. The resolved shear stress  $\tau^s$  is related to the corresponding viscoplastic shear rate  $\dot{\gamma}^s$  via a power law expression:

$$\dot{\gamma}^s = \left\{ \frac{|\tau^s - X^s| - R^s}{K} \right\}^n \text{sign}(\tau^s - X^s), \quad \text{with } \{a\} = \max(a, 0). \quad (3)$$

For each slip system, internal variables are introduced to describe the hardening of the material: isotropic hardening variables  $R^s$  and kinematic hardening variables  $X^s$ . In addition,  $n$  and  $K$  are the parameters controlling viscosity. The non-linear evolution rule for isotropic hardening involves a  $12 \times 12$  interaction matrix  $\mathbf{h}$  which includes self-hardening and latent hardening:

$$R^s = R_0 + Q \sum_u h_{su} [1 - \exp(-bv^u)], \quad \text{with } v^u = |\dot{\gamma}^u|, \quad (4)$$

where  $\mathbf{h}$  contains six independent parameters: one diagonal term (noted as  $h_1$ ) for the self-hardening and five other non-diagonal terms (i.e.  $h_2, h_3, h_4, h_5$  and  $h_6$ ) for the latent hardening. Also,  $R_0$  denotes the initial critical resolved shear stress (CRSS). The following non-linear kinematic hardening is also adopted:

$$X^s = C\alpha^s, \quad \text{with } \dot{\alpha}^s = \dot{\gamma}^s - D|\dot{\gamma}^s|\alpha^s. \quad (5)$$

Here, before loading,  $X^s = 0$ , thus  $\alpha^s$  is initialized as 0. Note that  $X^s$  tends to the saturated value  $C/D$  for large values of slip. The material parameters  $Q, b, C, D$  in the above equations must be identified for isotropic and kinematic hardening. The parameter identification for the single crystal model of Cu will be discussed in Section 4.1. Finally, plastic deformation  $\dot{\epsilon}_p^{(r)}$  in a crystal phase ( $r$ ) is the result of slip processes on all slip systems:

$$\dot{\epsilon}_p^{(r)} = \sum_{s=1}^{12} \dot{\gamma}^s \mathbf{m}^s. \quad (6)$$

### 3.2. Full-field periodic models

In the present work, a full-field FEM PH is proposed to compute the effective elasto-plastic behavior of Cu-Nb wires at the various scales. An elementary volume  $V$  made of heterogeneous materials is considered for polycrystalline aggregates (scale H0) in Section 3.2.1 and for hexagonal fiber assemblies (scales H1 and H2) in Section 3.2.2. Periodic boundary conditions are prescribed at the boundary  $\partial V$ . The displacement field  $\mathbf{u}$  in  $V$ , then takes the following form:

$$\mathbf{u}(\mathbf{x}) = \bar{\boldsymbol{\epsilon}} \cdot \mathbf{x} + \boldsymbol{\psi}(\mathbf{x}) \quad \forall \mathbf{x} \in V \quad (7)$$

where the fluctuation  $\boldsymbol{\psi}$  is periodic, i.e. it takes the same values at two homologous points on opposite faces of  $V$ . Furthermore, the traction vector  $\boldsymbol{\sigma} \cdot \mathbf{n}$  takes opposite values at two homologous points on  $\partial V$  ( $\mathbf{n}$  is the outwards normal vector to  $\partial V$ ). The finite element code used in this work ([Z-set package, 2013](#)) allows to prescribe the averaged strain components of  $\bar{\boldsymbol{\epsilon}}$ , or conjugate mean stress components ([Besson et al., 2009](#)).

#### 3.2.1. Full-field model for polycrystalline aggregates

As illustrated in [Fig. 3](#), Cu grains are highly elongated along  $x_1$  due to material processing, i.e.  $\ell/d \rightarrow \infty$ . In order to take this

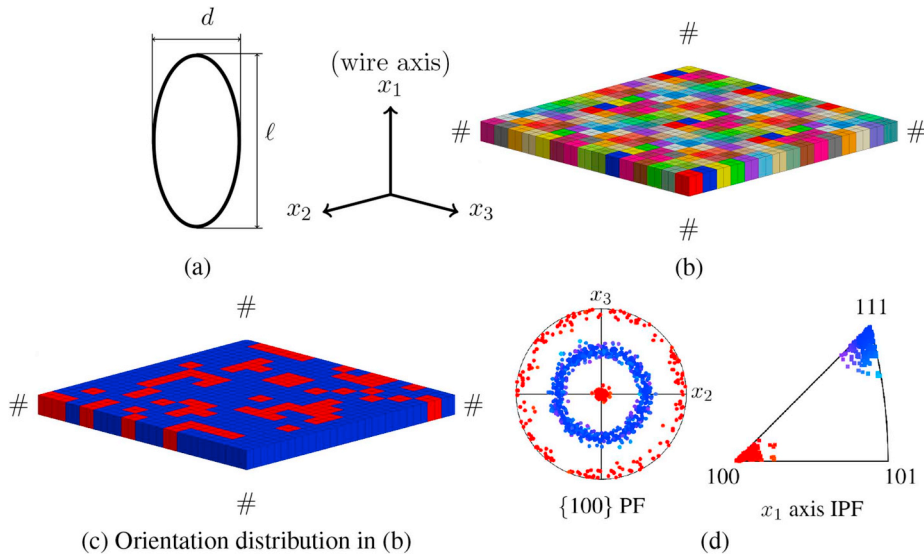


**Fig. 5.** FE meshes for columnar polycrystals: (a) The overall (mean) shape of a single grain elongated along direction  $x_1$  with dimensions  $\ell \times d \times d$ ; (b) Parallelepipedic tessellation of 225 grains ( $= 15 \times 15$ ) with the aspect ratio  $\ell/d \rightarrow \infty$  (periodic boundary conditions, denoted #, are considered); (c) Orientation distribution in the tessellation mesh (b), blue stands for  $\langle 111 \rangle$  fiber texture and red for  $\langle 100 \rangle$ ; (d)  $\{100\}$  Pole Figure and  $x_1$  axis Inverse Pole Figure of Cu-0. Grain orientations are generated by the software LaboTex based on experimental EBSD textures. (For interpretation of the references to color in this figure legend, the reader is referred to the Web version of this article.)

morphological texture into account, a slice-shaped parallelepipedic tessellation (finite element mesh using c3d20r elements, i.e. quadratic brick element with 20 nodes and reduced integration with 8 Gauss points) was proposed in Gu et al. (2017a), as shown in Fig. 5. This tessellation is composed of  $15 \times 15 (= 225)$  regularly arranged square grains, and it is subjected to periodic boundary conditions (Eq. (7)), thus taking advantage of a smaller RVE size than the one with homogeneous boundary conditions according to (Kanit et al., 2003). Furthermore, these 225 grain orientations obey the Orientation Distribution Function described in Section 2.2, and the discrete orientations are spatially randomly distributed among the grains of the parallelepipedic tessellation. Fig. 5 indicates the  $\langle 111 \rangle$  and  $\langle 100 \rangle$  fiber texture distributions, which are close to the EBSD orientation map of Fig. 2. The mesh density has also been selected as a compromise between numerical accuracy and computational time.

### 3.2.2. Full-field models for hexagonal fiber assemblies

The effective elasto-plastic behavior will be predicted for the hexagonal fiber assemblies of Cu-Nb composites at scales H1 and H2. As the specimens exhibit several characteristic scales, one of the modelling challenge is to account for the nonlinear behavior in the different scale transitions. This scale transition can be performed for elasto-(visco-)plastic heterogeneous materials with a complex and random microstructure in various ways, as mentioned Section 1. In this regard, macroscopic models, e.g. Haddadi et al. (2006) can provide an accurate homogenized behavior, however phenomenological parameter calibrations need to be repeated when the information at scale H0 changes. The FE<sup>2</sup> approach, e.g. (Feyel and Chaboche, 2000; Geers et al., 2010), required long CPU time despite applying parallel computational techniques. TFA/NTFA are promising models, e.g. (Michel and Suquet, 2016), and represent an alternative to the Finite Element method used in this work.

In the present work, in order to account for the elasto-(visco-)plastic behavior of hexagonal fiber assemblies of H1/H2 with a reasonable CPU time, a combination of the full-field FEM PH and the mean-field  $\beta$ -models is proposed, labeled as “Phi- $\beta$  model”

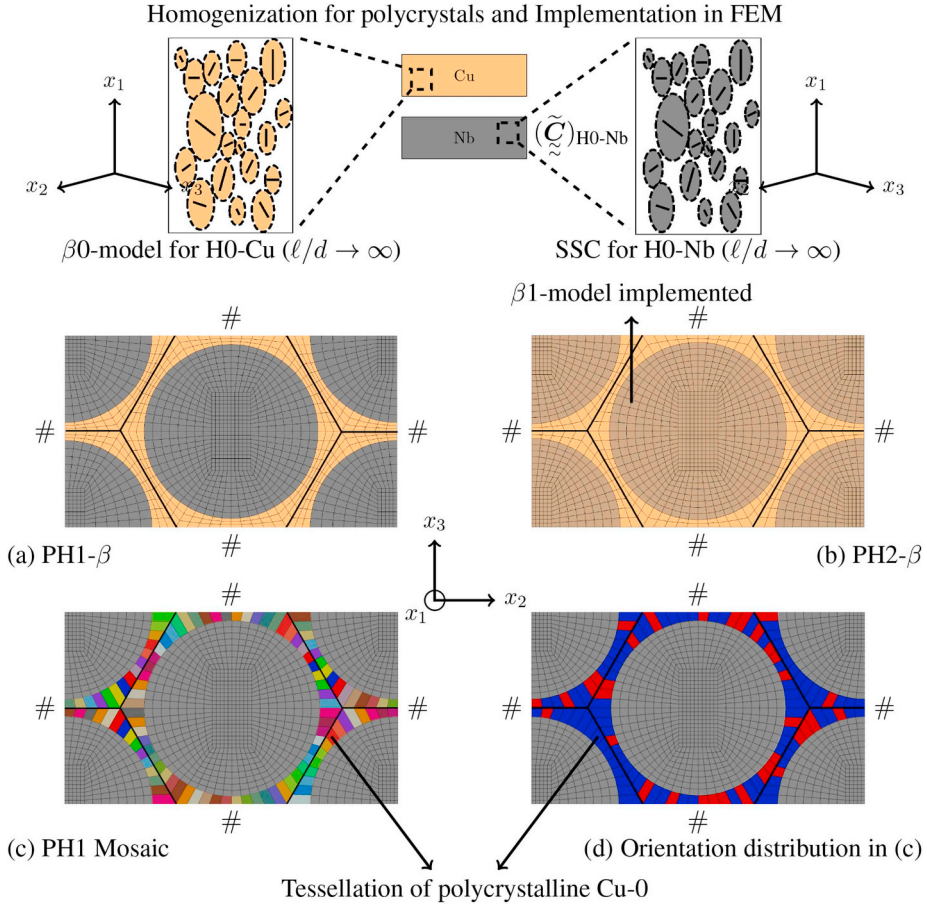


**Fig. 6.** Multiscale modeling of effective elasto-plastic behavior of Cu-Nb wires (Orange stands for Cu, gray for Nb, light gray for Cu-Nb composite): (a) Using the PH1- $\beta$  at scale H1, a periodic distribution of Nb fibers is assumed (# denotes periodic boundary conditions). The polycrystalline Nb and Cu-0 aggregates are described by an effective elastic stiffness obtained by the SSC scheme and an elasto-plastic behavior provided by the  $\beta_0$ -model, respectively (see the inset). (b) Using the PH2- $\beta$  at scale H2, the behavior of the Cu-Nb composite H1 zone is provided by the  $\beta_1$ -model, while that of the polycrystalline Cu-1 aggregate is given by a  $\beta_0$ -model accounting for the microstructure of Cu-1. (c) Using the PH1 Mosaic at scale H1, polycrystalline Cu-0 surrounding the elastic Nb is described by a tessellation of polycrystalline aggregates. (d) Orientation distribution in the tessellation of (c), blue stands for the  $\langle 111 \rangle$  fiber texture and red for  $\langle 100 \rangle$ .

( $i = 1, 2$  for scales H1 and H2 respectively). The section views of the unit cell at H1 and H2, with their meshes, are respectively indicated in Fig. 6(a) and Fig. 6(b). Inspired from the parallelepipedic tessellation of FEM for polycrystals, another “PH1 Mosaic” model is introduced, as shown in Fig. 6(c). These unit cells are subjected to periodic boundary conditions. They are composed of two equivalent long fibers ( $1 + 4 \times 1/4$  fibers) which are arranged in a hexagonal lattice, and they represent the (idealized) multi-scaled experimental microstructure of Cu-Nb wires. They contain all information about the morphological RVE at the effective scales H1 and H2.

Detailed descriptions of the above-mentioned models are as follows:

- In the *PH1- $\beta$  model*, Nb fibers are endowed with elastic properties with the effective stiffness tensor (denoted  $\left(\hat{\underline{c}}\right)_{\text{H0-Nb}}$ ) determined by the SSC scheme applied to pure Nb polycrystalline aggregate. These properties are taken from (Gu et al., 2017a). On the other hand, the mean-field  $\beta_0$ -model is used to estimate the effective elasto-plastic behavior of the pure polycrystalline Cu-0 aggregate with local nonlinear constitutive behavior described above, as illustrated in the upper insets of Fig. 6.
- Similarly, for the *PH2- $\beta$  model* at scale H2, the behavior of the H1 zone and of the Cu-1 surrounding matrix are provided to the  $\beta_1$ -model (random mix of Cu-0 and Nb grains) and  $\beta_0$ -model (aggregate of Cu-1 grains) respectively, as illustrated in Fig. 6(b). The  $\beta$ -models will be presented in Section 3.3 and their reliability will be demonstrated in Sections 4 and 5.
- The *PH1 Mosaic model* at H1 is composed of elastic Nb fibers and elasto-plastic Cu-0 channels. In these Cu-0 channels, individual grains are considered by a heterogeneous tessellation of polycrystalline aggregates, instead of a homogeneous medium used in the PH1- $\beta$  approach. Based on experimental observations as in Fig. 2, the transverse size  $d$  of Cu-0 grains varies from  $\delta/3$  to  $\delta$  where  $\delta$  denotes channel width of Cu. Here,  $d = \delta/2$  is chosen to construct the mesh. The experimental  $\langle 111 \rangle$  and  $\langle 100 \rangle$  fibers textures are taken into account. Therefore, the tessellation of polycrystalline Cu-0 is able to account for the accurate information of crystallographic/morphological textures. In this work, we regard the responses of the PH1 Mosaic model as benchmarks at scale H1.

Note that FEM PH models describe an infinite periodic honeycomb microstructure. However, the real architecture of Cu-Nb wires at all scales contains only a finite number (i.e. 85) of long fibers. Simulations of a larger hexagonal structure without periodic boundary conditions have been performed to check that the hypothetical periodicity does not significantly affect the results. Furthermore, the mesh density for the models at H1/H2 will receive further attention in Section 5.2, due to strain localization phenomena occurring in the Cu matrix. Finally, it is noted that the calculations (including all the full-field approaches in this work) require a 2D analysis with generalized plane strain conditions in order to allow for homogeneous strain in the third direction and out of plane shearing. For that purpose, a 3D mesh with one single element in the thickness is used, together with suitable boundary conditions to keep flat upper and lower planes.

### 3.3. Mean-field $\beta$ -model

The full-field PH1- $\beta$  model for hexagonal fiber assemblies at scale H1 requires a local constitutive law to describe the elasto-plastic behavior of polycrystalline Cu-0 matrix (similarly for PH2- $\beta$ ). In this regard, the mean-field method is used to estimate the effective behavior of polycrystalline materials at H0 and the found model is implemented in FEM as a polycrystalline constitutive law at H1. The mean-field approaches are often advocated to be CPU time saving models for polycrystalline aggregates, compared with FEM (Prakash and Lebensohn, 2009). Among a wealth of literature references for the mean-field schemes mentioned in Section 1, the  $\beta$ -models (Cailletaud and Coudon, 2016; Coudon et al., 2018) are chosen in the present work, due to (1) its higher computational efficiency compared to other semi-analytical schemes, e.g. Turner and Tomé (1994) and (2) its suitability for the anisotropic behavior of multi-axial polycrystals. (1) is particularly beneficial for the iterative scale transition processes, as the PHi- $\beta$  ( $i = 1, 2$ ) like models consume a lot of computational resources (Geers et al., 2010). Concerning (2), this model is suited for both Cu and Nb grains exhibiting highly elongated grains (i.e.  $\ell \gg d$ ).

In this work, the  $\beta$ -models are categorized into two types, accounting for the various scales (see appendix A for the detailed formulation of the  $\beta$ -model):

- *$\beta_0$ -model*. At scale H0,  $\beta$ -model can be used to describe the elasto-plastic behavior of polycrystalline aggregates made of pure Cu grains. In this work, the  $\beta_0$ -model takes into account three different Cu components, labeled “ $\beta_0$ -model for H0-(Cu- $i$ ) ( $i = 0, 1, 2$ )”.
- *$\beta_i$ -model ( $i = 1, 2$ )*. The  $\beta_1$ -model constructs a fictitious material in which Cu and Nb grains are randomly mixed together, with the volume fractions, textures, grain size dependent yield stress  $\sigma_y$ , and initial residual stresses  $\sigma_{\text{res}}$  at H1 accounted for, but without considering the periodic architecture. In this way, the  $\beta_1$ -model predicts the elasto-plastic behavior at scale H1. Similarly, the  $\beta_2$ -model takes into account the microstructural information at H2, however without considering anymore the specific architecture (i.e. hexagonal fiber assemblies) of Cu-Nb wires. The predictive capability and computational efficiency of the proposed  $\beta_i$ -models ( $i = 1, 2$ ) will be discussed in Section 5. The proposition of such a model is based on findings of Gu et al. (2017a) in which it has been shown that the mean-field SSC scheme reliably estimates the effective elastic behavior of Cu-Nb wires not only at scale H0, but also at scales H1/H2 assuming a sole random mixture of Cu/Nb grains.

Hereafter, a *mechanical phase* ( $r$ ) denotes the set of all grains in the microstructure that exhibit the same crystal orientation with a given precision; those grains have however different shapes and environment. The scale transition interaction equation of  $\beta$ -models is

the following (see [Appendix A](#) for the detailed derivation and corresponding assumptions):

$$\boldsymbol{\sigma}^{(r)} = \underline{\underline{\mathbf{B}}}^{(r)} : \left[ \bar{\boldsymbol{\sigma}} + \underline{\underline{\mathbf{L}}}_c^* : (\tilde{\boldsymbol{\beta}} - \boldsymbol{\beta}^{(r)}) \right] + \boldsymbol{\sigma}_{\text{res}}^{(r)} \quad (8)$$

where  $\underline{\underline{\mathbf{B}}}^{(r)}$  and  $\boldsymbol{\sigma}_{\text{res}}^{(r)}$  denote respectively the stress concentration tensor (estimated according to the elastic SSC scheme) and the initial residual stress in phase  $(r)$ . It provides the mean stress in each phase  $(r)$  as a function of the overall stress  $\bar{\boldsymbol{\sigma}}$  and of the plastic accommodation variables  $\boldsymbol{\beta}^{(r)}$ . The stress heterogeneity from phase to phase results from the deviation of the  $\beta$ -variables  $\boldsymbol{\beta}^{(r)}$  from their effective value  $\tilde{\boldsymbol{\beta}}$  (see [Appendix A](#)). The accommodation tensor  $\underline{\underline{\mathbf{L}}}_c^*$  is expressed as:

$$\underline{\underline{\mathbf{L}}}_c^* = \underline{\underline{\mathbf{C}}}: \left( \underline{\underline{\mathbf{I}}} - \underline{\underline{\mathbf{S}}}_{\text{Esh}} \right) \quad (9)$$

with  $\underline{\underline{\mathbf{I}}}$  the fourth order identity tensor and  $\underline{\underline{\mathbf{S}}}_{\text{Esh}}$  the Eshelby tensor for spheroidal inclusions with ratio  $\ell/d$ . Here,  $\underline{\underline{\mathbf{S}}}_{\text{Esh}}$  depends on the effective stiffness tensor  $\underline{\underline{\mathbf{C}}}$  (instead of the elasto-plastic tensor  $\underline{\underline{\mathbf{L}}}$  as in Hill's proposition) and on the morphological texture  $\ell/d$ . In order to correct the errors caused by the assumption of using only the elastic behavior for determining  $\underline{\underline{\mathbf{L}}}_c^*$ , the variables  $\boldsymbol{\beta}$  introduce a plastic accommodation associated with plastic strain tensors  $\boldsymbol{\varepsilon}_p^{(r)}$  in each phase. The evolution equation for the  $\beta$ -variables reads:

$$\dot{\boldsymbol{\beta}}^{(r)} = \dot{\boldsymbol{\varepsilon}}_p^{(r)} - \underline{\underline{\mathbf{D}}}: \boldsymbol{\beta}^{(r)} \|\dot{\boldsymbol{\varepsilon}}_p^{(r)}\| \quad (10)$$

where  $\dot{\boldsymbol{\varepsilon}}_p^{(r)}$  denotes the von Mises equivalent plastic strain rate. Analogous to  $\boldsymbol{\varepsilon}_p^{(r)}$ ,  $\boldsymbol{\beta}^{(r)}$  variables are initialized as  $\mathbf{0}$  before loading. The evolution equation (10) is similar to a nonlinear kinematic hardening rule ([Besson et al., 2009](#)). In this equation,  $\underline{\underline{\mathbf{D}}}$  denotes a fourth order phenomenological constant tensor to be calibrated, in such a way that the  $\beta$ -model responses fit the stress-strain curve obtained by the benchmark FEM (as indicated in the algorithm of [Fig. 4](#)). It means that the FEM unit cell simulations serve as input data for the calibration of some parameters of the  $\beta$ -models. These models can therefore be seen as reduced order models driven by explicit evolution equations, instead of integral differential equations very often encountered in more classical homogenization methods. This model feature contributes to CPU time saving, the price to pay being the calibration of the scale transition coefficients. In this work, the tensor  $\underline{\underline{\mathbf{D}}}$  is assumed to have constant values irrespective of the phase  $(r)$ . It admits  $x_1$  as a symmetry axis and takes the form:

$$\underline{\underline{\mathbf{D}}} = \begin{pmatrix} D_{11} & D_{12} & D_{12} & & & \\ D_{12} & D_{33} & D_{23} & & & \\ D_{12} & D_{23} & D_{33} & & & \\ & & & D_{44} & & \\ & & & & D_{55} & \\ & & & & & D_{55} \end{pmatrix}. \quad (11)$$

which is similar to the form also used in ([Sai et al., 2006](#); [Martin et al., 2014](#)) for columnar grain morphology. In the material frame, assuming the deviatoric property of the accommodation variable, i.e.  $\text{trace}(\boldsymbol{\beta}^{(r)}) = 0$ , the following additional condition is enforced according to Eq. (10) ([Sai et al., 2006](#)):

$$D_{11} = D_{33} + D_{23} - D_{12}. \quad (12)$$

Therefore, there are five independent coefficients  $D_{ij}$  to be determined, see Section 4.3 for the corresponding identification strategy.

Finally, the definition of the overall variable  $\tilde{\boldsymbol{\beta}}$  in Eq. (8) is derived from the homogenization condition  $\bar{\boldsymbol{\sigma}} = \langle \boldsymbol{\sigma}^{(r)} \rangle$ , which gives

$$\tilde{\boldsymbol{\beta}} = \langle \underline{\underline{\mathbf{L}}}_c^{*-1} : \underline{\underline{\mathbf{B}}}^{(r)} : \underline{\underline{\mathbf{L}}}_c^* : \boldsymbol{\beta}^{(r)} \rangle. \quad (13)$$

### 3.4. Statistical representative volume element

When a single realization over the elementary volume  $V$  (e.g. polycrystalline aggregates at HO) is used, a relatively limited number of grain orientations and grain neighborhoods are accounted for. This leads to a bias in the estimation of the effective properties, as explained in ([Kanit et al., 2003](#)). The RVE must contain a sufficiently large number of heterogeneities (e.g., grains, inclusions, fibers etc.) for the macroscopic properties to be independent of the boundary conditions applied to this volume. [Kanit et al. \(2003\)](#) proposed a statistical strategy to determine the RVE size for elastic moduli.

In this work, this approach is extended to elasto-plasticity by considering  $n$  realizations of the microstructure in a volume with given size. This volume size is then increased to investigate the asymptotic elasto-plastic stress (or strain):

$$\bar{Z}(t) = \frac{1}{n} \sum_{i=1}^n \tilde{Z}_i(t), \quad D_Z(t)^2 = \frac{1}{n} \sum_{i=1}^n [\tilde{Z}_i(t) - \bar{Z}(t)]^2 \quad (14)$$

where  $\tilde{Z}_i(t)$  is an apparent elasto-plastic stress (or strain) obtained for one realization, and  $\bar{Z}(t)$  is its mean value over  $n$  realizations at a given time  $t$  during loading. The variance  $D_Z(t)^2$  denotes the fluctuations of  $\tilde{Z}_i(t)$ . The number of realizations  $n$  is chosen so that the

obtained mean value  $\bar{Z}(t)$  does not vary any longer up to a given precision when  $n$  is increased. This precision (i.e. relative error  $\varepsilon_{\text{rela}}(t)$ ) of the estimation of the effective property  $\bar{Z}(t)$  is related to the standard deviation  $D_Z(t)$  and the number of realizations  $n$  by:

$$\varepsilon_{\text{rela}}(t) = \frac{2D_Z(t)}{\sqrt{n}\bar{Z}(t)}. \quad (15)$$

Conventionally, if at any time  $t$  during the loading path,  $\varepsilon_{\text{rela}}(t) \leq 1.5\%$ , we consider that the RVE size is reached. The overall effective elasto-plastic response is then defined by the mean value over  $n$  realizations,  $\bar{Z}(t)$  and the 95% confidence interval is given by  $[\bar{Z}(t) - 2D_Z(t), \bar{Z}(t) + 2D_Z(t)]$ .

From the Orientation Distribution Function described in Section 2.2, four sets of 10000 discrete orientations (for Cu-0, Cu-1, Cu-2 and Nb) are created by LaboTex.<sup>2</sup> They are used to generate the microstructures for the full-field/mean-field scale transition models. At scale H0, for the FEM for polycrystalline aggregates, 20 realizations were performed and found to fulfill the statistical requirements for all the loading conditions considered in this work. This corresponds to a total of 4500 (20×225) crystallographic orientations chosen randomly from the full data set. In addition, 95% confidence intervals for the average stress  $\bar{\sigma}$  (and average strain  $\bar{\varepsilon}$ ) deduced from these realizations will be plotted hereafter by error bars. Note that strain intervals will only be shown at the ultimate loading stage for the sake of clarity. At scale H1, the statistical RVE still requires 20 realizations for the PH1 Mosaic model, i.e. 2400 (20 × 120) crystallographic orientations of Cu-0. For the PH1- $\beta$  model, as a compromise between precision and CPU time, 120 grain orientations are considered in a single realization for the  $\beta$ 0-model which serves as the local constitutive behavior of H0-(Cu-0). Here, 20 realizations are required for the PH1- $\beta$  model, the same as in the PH1 Mosaic model. At H2, 20 realizations are also performed for the PH2- $\beta$  model in which the  $\beta$ 1-model and  $\beta$ 0-model take into account 240 orientations (120 for Cu-0, 120 for Nb) and 120 orientations (for Cu-1) respectively. Furthermore, the same number of orientations (RVE size) is used in the mean-field  $\beta$ -models at all scales as in the corresponding full-field models. It turns out that, in contrast to the full-field simulations, the results of  $\beta$ -models display negligible scatter, probably due to the large number of grain orientations considered. For example, at H0, the  $\beta$ 0-model includes for 4500 orientations, the same as the total number of grains considered in FEM for polycrystalline aggregates. The uncertainty related to statistical RVE size (i.e. the error bars in the homogenized stress-strain curves) will be shown in Section 4 and Section 5 for the model responses at H0 and at H1/H2 respectively.

## 4. Homogenization at scale H0

### 4.1. Parameter identification for the single crystal plasticity model

This section is devoted to the homogenization at scale H0, i.e. to the estimation of effective behavior of polycrystalline Cu and Nb aggregates separately. Table 3 provides the cubic elastic constants  $\tilde{\mathcal{C}}$  (Voigt convention) of Cu and Nb single crystals. Previously, Gu et al. (2017a) has already predicted the effective elastic properties of Cu-Nb wires at various scales via SSC homogenization scheme, accounting for the specific morphological/crystallographic textures. These model results were validated systematically by both macroscopic tensile tests and in-situ diffraction data with a good agreement. For the polycrystalline Nb at H0, its five effective elastic moduli in the transverse isotropic stiffness  $\left(\tilde{\mathcal{C}}\right)_{\text{H0-Nb}}$  are reported in Table 3, based on Gu et al. (2017a). These elastic properties are used as the local behavior of Nb fibers in PH1- $\beta$  and PH1 Mosaic models.

We now proceed to the estimation of the effective elasto-plastic behavior of Cu polycrystals. At first, the model parameters for the single crystal plasticity will be identified, then these parameters will be used for Cu-Nb composite wires. In this work, the experimental stress-strain curve of a pure highly hardened OFHC Cu wire is chosen as the reference copper behavior. These pure Cu wires were obtained by severe cold-drawing at room temperature, the diameter of cylindrical sample was reduced from 15 mm to 0.29 mm. It should be noticed that, at the end of fabrication steps, Cu-Nb wires experience a similar process, i.e. supplementary cold-drawing. Thus, it is believed that the pure highly hardened OFHC Cu exhibits a mechanical behavior similar to the Cu components in Cu-Nb wires.

Both EBSD and tension experiments for the pure Cu wires were carried out at Centre des Matériaux Mines ParisTech. It was found that the pure Cu wires exhibit a  $\langle 111 \rangle$ - $\langle 100 \rangle$  (50% for each) double fiber texture and elongated grain shape with respect to  $x_1$  axis, which is similar to the crystallographic/morphological textures of Cu components in Cu-Nb wires. Monotonic tensile tests along  $x_1$  were performed with a strain rate  $\dot{\varepsilon} \approx 5 \times 10^{-5} \text{ s}^{-1}$  at 293 K. In an effort to determine the total specimen strain with a high accuracy during the tensile test on the wire, the Digital Image Correlation (DIC) technique was used, see e.g. Pan et al. (2009). Fig. 7 shows the experimental results of the tensile test. The data processing of 2D DIC leads to an uncertainty  $< \pm 0.02\%$  for the longitudinal strain. The stress values are computed from the tensile force and the corresponding uncertainty is estimated as  $\pm 15 \text{ MPa}$  due to stress relaxation during image acquisition. Moreover, the macroscopic longitudinal Young's modulus  $E_1$  and yield stress  $\sigma_y$  (with a conventional criterion of 0.02% plastic strain) along the wire direction  $x_1$  are found respectively to be  $\sim 130 \text{ GPa}$  and  $\sim 350 \text{ MPa}$ . Thus, the pure Cu wires display a similar yield stress compared with the Cu components in Cu-Nb wires estimated in Section 2.4. Finally, the specimen breaks at an applied strain  $\sim 1.2\%$ .

Several authors have identified some parameters of the single crystal Méric-Cailletaud model for recrystallized OFHC copper, generally with grain size  $\sim 100 \mu\text{m}$ , in various situations: Cu bicrystals under cyclic tension-compression with  $\varepsilon^{\text{min,max}} = \pm 0.1\%$  and

<sup>2</sup> Software for crystallographic textures - <http://www.labosoft.com.pl/>.

**Table 3**

Model parameters used in this work for elasticity, single crystal plasticity and the  $\beta$ -models. The notations and values for the independent moduli of the transverse isotropic H0-Nb material are taken from [Gu et al. \(2017a\)](#). The same parameter combination of  $D_{ij}$  is chosen for all the  $\beta$ -models at all scales. The CRSS  $R_0$  is 118.0 MPa for Cu-1 and Cu-2 polycrystalline aggregates but rises to 170 MPa for Cu-0 due to size effects ( $\delta = 310$  nm).

Elasticity						
	$C_{11}$ (GPa)		$C_{12}$ (GPa)		$C_{44}$ (GPa)	
Cu	167.2		120.7		75.7	
Nb	245.6		138.7		29.3	
$\left(\begin{smallmatrix} \tilde{\nu} \\ \tilde{\mu} \end{smallmatrix}\right)_{\text{H0-Nb}}$						
	$\tilde{E}_1$ (GPa)		$\tilde{\nu}_{12}$		$\tilde{K}_{23}$ (GPa)	$\tilde{\mu}_{12}$ (GPa)
	95.9		0.408		185.7	39.5
						$\tilde{\mu}_{23}$ (GPa)
						37.0
Single crystal plasticity						
Isotropic hardening			Kinematic hardening		Viscosity	
$Q$ (MPa)	$b$	$R_0$ (MPa)	$C$ (MPa)	$D$	$K$ (MPa $\cdot\cdot^{1/n}$ )	$n$
6.0	15.0	118.0 or 170.0	4500.0	600.0	2.0	15.0
$h_1$	$h_2$		$h_3$	$h_4$	$h_5$	$h_6$
1.0	4.4		4.75	4.75	4.75	5.0
$\tilde{D}$ in $\beta$ -models ( $D_{11} = D_{33} + D_{23} - D_{12}$ , other components are zero)						
$D_{11}$	$D_{12}$		$D_{23}$	$D_{33}$	$D_{44}$	$D_{55}$
200	200		185	215	70	240

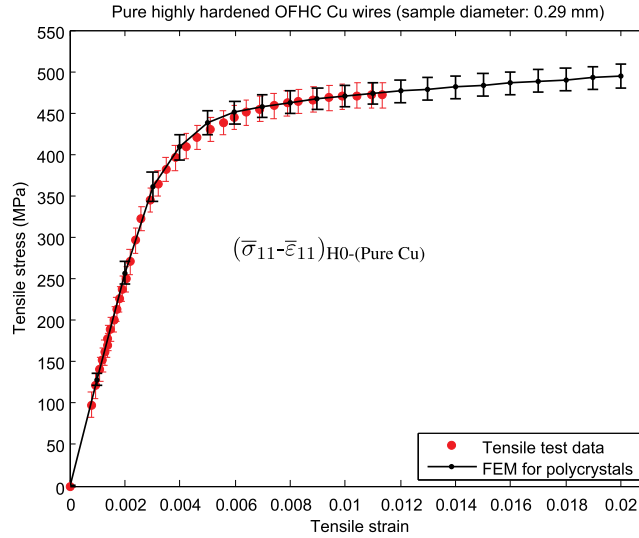


**Fig. 7.** Identification of phenomenological parameters for single crystal plasticity: FEM results are compared to experimental data for the pure highly hardened OFHC Cu aggregate.

$\pm 0.5\%$  ([Méric et al., 1994](#)); Cu polycrystals under monotonic tension with  $\bar{\epsilon}^{\max}$  up to 10% and under cyclic loading with  $\bar{\epsilon}^{\min, \max} = \pm 0.5\%$  ([Šiška et al., 2006](#); [Musienko et al., 2007](#)); Textured Cu polycrystals under cyclic loading with  $\bar{\epsilon}^{\min, \max} = \pm 1.0\%$  ([Gérard, 2008](#); [Gérard et al., 2013](#)). In the present work, the values  $Q$ ,  $b$ ,  $C$ ,  $D$  and  $h_{ij}$  (interaction matrix) found by [Musienko et al. \(2007\)](#) are chosen as initial estimation. In fact, the combination of parameters by [Gérard \(2008\)](#) leads to similar results. In the case of quasi-static mechanical tests (strain rate  $\dot{\epsilon} < 10^{-2} \text{ s}^{-1}$ ) at 293 K, strain rate sensitivity of OFHC Cu is negligible ([Meyers et al., 1995](#); [Lu et al., 2001](#)). Viscosity parameters  $K$  and  $n$  are assigned to  $2.0 \text{ MPa} \cdot \text{s}^{1/n}$  and 15.0 respectively. Recrystallized OFHC copper studied in [Musienko et al. \(2007\)](#) exhibits a yield stress  $\sigma_y \sim 10$  MPa much smaller than the one estimated in our case ( $\sigma_y$  up to 350 MPa). In this work,  $R_0$  is identified as 118.0 MPa by fitting the model responses of FE polycrystals to the tensile test data, with a satisfactory match, see [Fig. 7](#). As for Cu-0 ( $\delta = 310$  nm), an even higher yield stress of 500 MPa is estimated, due to the grain size effects. This requires a

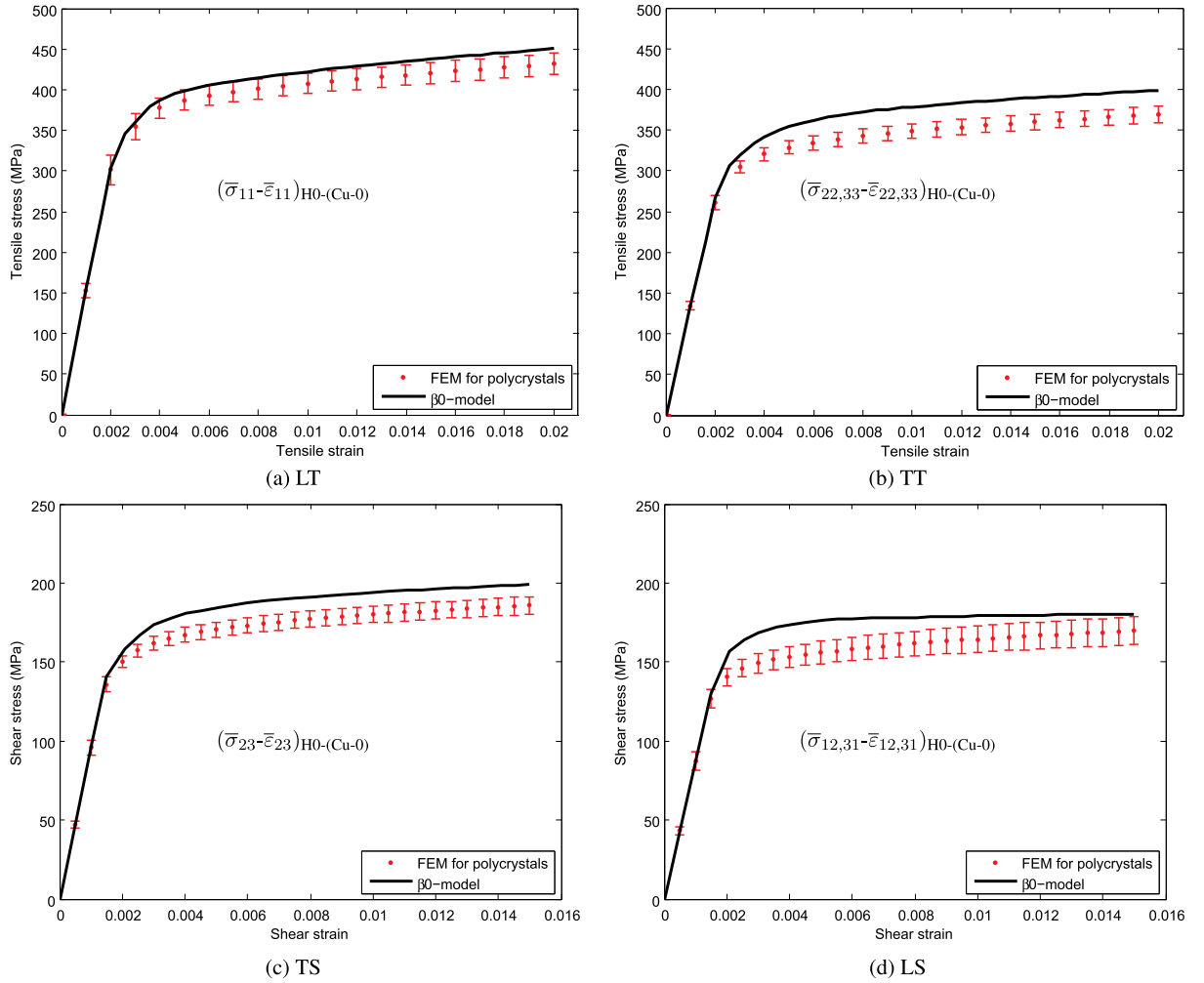


**Fig. 8.** Effective elasto-plastic behavior of the polycrystalline Cu-0, i.e. at scale H0-(Cu-0), obtained by the FEM for polycrystals and the  $\beta$ -model. Various loading conditions are presented: (a) Longitudinal Tensile (LT) test, (b) Transverse Tensile (TT) test, (c) Transverse Shear (TS) test and (d) Longitudinal Shear (LS) test. See Section 4.2 for the conventions of loading conditions.

CRSS  $R_0$  of 170 MPa. All the model parameters of single crystal plasticity are summarized in Table 3. Except for  $R_0$ , Cu-0, Cu-1 and Cu-2 in Cu-Nb wires will share the same parameter combination.

#### 4.2. Results of FEM for polycrystals

In this section, the simulation results obtained by FEM for Cu polycrystals are provided. They will be served as references for the parameter identification of the  $\beta$ -model. Results are provided considering the crystallographic texture of Cu-0 indicated in Table 2 and single crystal parameters indicated in Table 3 with  $R_0 = 118$  MPa (i.e.  $\sigma_y = 350$  MPa corresponding to  $\delta = 2.19 \mu\text{m}$ ). Taking into account the expected transverse anisotropic behavior, the four following loading conditions of the RVE are successively considered:

- $\bar{\epsilon}_{11} = 2\%$  for the Longitudinal Tensile test (denoted LT hereafter);
- $\bar{\epsilon}_{22} = 2\%$  or  $\bar{\epsilon}_{33} = 2\%$  for the Transverse Tensile tests (TT);
- $\bar{\epsilon}_{23} = 1.5\%$  for the Transverse Shear test (TS);
- $\bar{\epsilon}_{12} = 1.5\%$  or  $\bar{\epsilon}_{31} = 1.5\%$  for the Longitudinal Shear test (LS).

Fig. 8 shows successively the volume average stress-strain curves at scale H0-(Cu-0) for the four loading conditions. In TT loaded along  $x_2$  or  $x_3$ , the model responses are similar. For a single microstructure realization, the deviation  $\epsilon_{\text{rela}}$  is not negligible ( $\sim 5\%$ ) due to the limited number of crystallographic orientations considered. Therefore, 225 grains are not sufficient to constitute an accurate RVE. TT results are thus determined by the average model responses along  $x_2$  and  $x_3$  directions. A similar procedure is used for LS tests. Furthermore, in order to investigate the heterogeneities of model response at H0-(Cu-0), Fig. 9 shows the average stress-strain

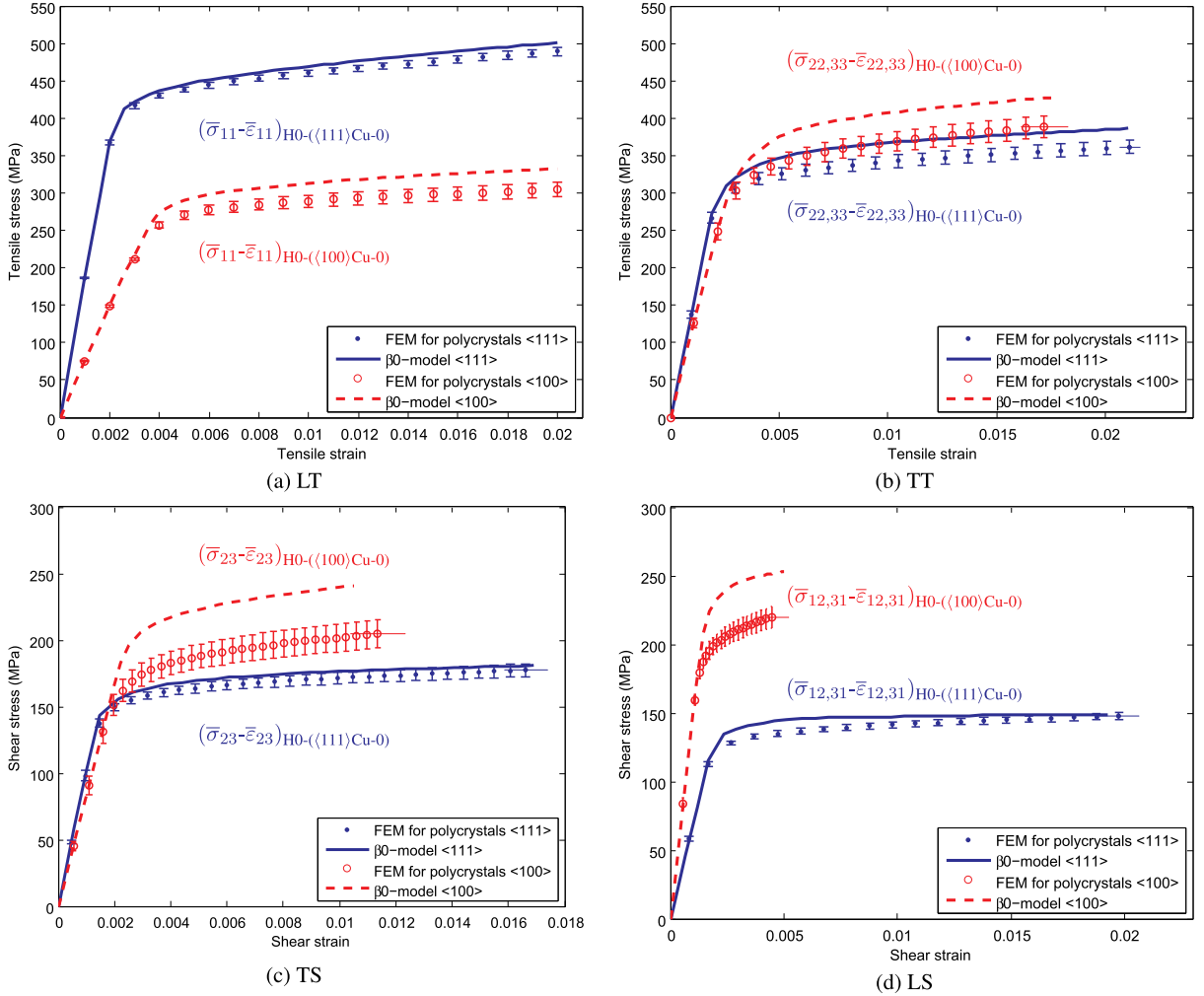


**Fig. 9.** Effective behavior of the individual  $\langle 111 \rangle$  and  $\langle 100 \rangle$  fiber textures at scale H0-(Cu-0), obtained by the FEM for polycrystals and the  $\beta_0$ -model. Various loading conditions are considered: (a) LT, (b) TT, (c) TS and (d) LS tests. Blue stands for the  $\langle 111 \rangle$  fiber texture and red for  $\langle 100 \rangle$ . (For interpretation of the references to color in this figure legend, the reader is referred to the Web version of this article.)

of  $\langle 100 \rangle$  and  $\langle 111 \rangle$  fiber components separately (denoted  $(\bar{\sigma} - \bar{\epsilon})_{H0-(\langle 100 \rangle Cu-0)}$  and  $(\bar{\sigma} - \bar{\epsilon})_{H0-(\langle 111 \rangle Cu-0)}$  respectively).

As shown in Fig. 8(a) and (b), an anisotropic response at H0-(Cu-0) is observed, the effective behavior in LT displaying a stronger response than the one in TT. Yield stresses of LT and TT are about 355 MPa and 300 MPa respectively. Fig. 9(a) and (b) reveal that the  $\langle 111 \rangle$  fiber exhibits higher stress levels than the  $\langle 100 \rangle$  fiber in LT. Conversely,  $\langle 100 \rangle$  fibers tend to be stronger than  $\langle 111 \rangle$  ones in TT. Also, the anisotropic effective Young's moduli of polycrystals Cu and the ones of individual fiber texture components can be found in Gu et al. (2017a). In LT, all the grains experience the same axial strain so that plastic activity occurs in  $\langle 100 \rangle$  oriented grains at a higher strain  $\bar{\epsilon}_{11}$  (also, at a higher applied stress  $\bar{\sigma}_{11}$ ) than in  $\langle 111 \rangle$  ones, as illustrated in Fig. 9(a). On the other hand, the yield stress of  $\langle 111 \rangle$  is higher than  $\langle 100 \rangle$ , displaying about 420 MPa and 270 MPa respectively. This phenomenon will receive further attention for analyzing experimental data in Section 6.4.

#### 4.3. Parameter identification for the $\beta$ -models

The previous FEM full-field results at H0-(Cu-0) for polycrystals now serve as references for the identification of the mean-field  $\beta_0$ -model. The parameters to be identified are limited to the components of the phenomenological tensor  $\underline{\underline{D}}$  appearing in Eq. (10). All the test responses LT, TT, TS and LS discussed in the previous section are used for the identification process of the  $\beta_0$ -model. It is found that the parameters  $D_{11}$ ,  $D_{12}$ ,  $D_{23}$  and  $D_{33}$  can be calibrated from the LT and TT overall responses. Moreover,  $D_{44}$  and  $D_{55}$  control respectively the responses for TS and LS. Optimal values for  $D_{44}$  and  $D_{55}$  can be found, but the combination of  $D_{11}$ ,  $D_{12}$ ,  $D_{23}$  and  $D_{33}$  is not unique, despite additional constraints have been introduced with Eq. (12). Here, a value  $D_{11}$  is chosen to have a similar magnitude than  $D_{55}$ . All the non-zero components in  $\underline{\underline{D}}$  are reported in Table 3.

As illustrated in Figs. 8 and 9, it is remarkable that the FEM for polycrystals and the  $\beta_0$ -model responses at H0-(Cu-0) are in a

general good agreement, not only for the effective behavior, but also for the average behavior of each individual fiber texture components. These results demonstrate that the fast computing  $\beta_0$ -model is an efficient homogenization tool for polycrystals at H0. However, an overestimation of hardening by the  $\beta_0$ -model is observed in Fig. 9 compared with the reference, especially for the  $\langle 100 \rangle$  fiber, with differences up to  $\sim 15\%$ , in TT, TS and LS. Conversely, the deviation between the FEM and the  $\beta_0$ -model responses in LT is rather small,  $\sim 5\%$ . We have checked that different  $D_{ij}$  combinations will not reduce this deviation, showing that the found set of parameters is a compromise with respect to the quality of stress prediction for the various tests. The limitations of  $\beta$ -model must be related to simplicity of the explicit scale transition rule Eq. (8). In particular, it is believed that the observed error is mainly caused by the fact that the considered elastic interaction (as in Kröner's approach) is not fully corrected by the introduction of internal variables  $\beta$ . This feature is amplified by the high contrast between the stress responses of the individual fiber textures.

The  $\beta_0$ -model is also used to describe the elasto-plastic behavior of Cu-1 and Cu-2 which have different textures. Based on the values calibrated for Cu-0, the parameters  $\underline{D}$  can still be slightly modified for various Cu components. However, very limited improvement is found by using  $\underline{D}$  calibrated specially for Cu-1 or Cu-2. Similarly,  $\underline{D}$  can also be slightly modified for the  $\beta_1$ -model and  $\beta_2$ -model, with again limited improvement. Thus, for the sake of simplicity, the same parameter combination  $D_{ij}$  is chosen for all the  $\beta$ -models at all scales.

## 5. Scale transitions up to H1 and H2 for architected Cu-Nb composites

Iterative scale transition steps are now performed up to H1 and H2 scales for the Cu-Nb wires arranged in multiscale hexagonal fiber assemblies. In Section 5.1, the results at scale H1 obtained by full-field PH1- $\beta$  and PH1 Mosaic models and mean-field  $\beta_1$ -model are provided. The comparison of model responses reveals a good agreement, however differences between these models are still observed, up to  $\sim 15\%$  in some cases. In Section 5.2, the main factors that contribute to these deviations are analyzed. In Section 5.3, based on the models at scale H1, scale transition steps up to H2 accounting for elasto-plasticity are proposed (i.e. PH2- $\beta$  and  $\beta_2$ -model). Finally, in Section 5.4, the error propagation within a hierarchical multiscale modeling approach is discussed. This leads to the selection of the best-suited modeling strategy for Cu-Nb composite wires.

### 5.1. Results at scale H1

The mean-field  $\beta_0$ -model has been demonstrated to be an efficient homogenization tool to describe the effective elasto-plastic behavior of pure polycrystalline Cu, in Section 4.3. Now, we proceed to the homogenization of the assembly of 85<sup>1</sup> elementary long fibers, i.e. scale H1. The PH1- $\beta$  approach takes the  $\beta_0$ -model as local constitutive law for the Cu-0 matrix in the FE computation. In addition, an alternative PH1 Mosaic model is proposed which takes the copper matrix as a grain microstructure directly. Both full-field PH1- $\beta$  and PH1 Mosaic models account for a periodic Cu-Nb hexagonal fiber distribution. Besides, in order to save CPU time and to perform the scale transitions from H1 to H2, the simple mean-field  $\beta_1$ -model will be used assuming a microstructure consisting of the sole random mixture of Cu and Nb phases (Section 3.3).

In Fig. 10, the effective elasto-plastic behavior at H1 is predicted by these three homogenization approaches for the LT, TT, TS and LS tests. A good agreement is seen among the model responses at H1, even though deviations are observed, e.g. the  $\beta_1$ -model displays a flatter plastic behavior in TS and LS, compared with the other two full-field model responses. In order to investigate the origins of these discrepancies and to study the heterogeneities of model responses among the phases, stress-strain curves of each individual component at H1, i.e. Nb and Cu-0, are plotted in Fig. 11. It is remarkable that all these three models provide generally close results for both the effective behavior at H1 and the "local" behavior of each individual component. The deviations among models will receive further attention in Section 5.2.

For the LT test, the effective longitudinal Young's modulus is found to be  $\sim 110$  GPa (97 GPa for Nb and 149 GPa for Cu-0). Once plastic activity occurs in Cu-0, the effective tangent modulus at H1 becomes  $\sim 73$  GPa. The tensile stress of Nb component is as large as  $\sim 2$  GPa when  $(\bar{\epsilon}_{11})_{H1-Nb} = 2\%$  is imposed. In addition for LT, all components are subjected to a uniform longitudinal strain, i.e.  $(\bar{\epsilon}_{11})_{H1} = (\bar{\epsilon}_{11})_{H1-Nb} = (\bar{\epsilon}_{11})_{H1-(Cu-0)}$ . This is because the microstructure is made of elongated Nb fibers/Cu-0 tubes, and these components are deformed in parallel along the longitudinal direction. On the other hand, in TT, TS and LS, strains in Nb/Cu-0 components are not uniform due to the heterogeneous architecture at H1, and also due to the property contrast between elastic Nb and elasto-plastic Cu-0. At the ultimate loading stage, Cu-0 undergoes an average strain up to  $\sim 5\%$ ; in contrast, average strain in Nb is as small as  $\sim 1\%$  for TT and  $\sim 0.5\%$  for TS and LS.

### 5.2. Strain localization phenomena for shear loading conditions

The largest discrepancy between the responses of the H1 of PH1 Mosaic, PH1- $\beta$  and  $\beta_1$ -models is found for transverse shear loading (TS), as it can be seen from Fig. 10(c) and Fig. 11(c). Both full-field PH1 Mosaic and PH1- $\beta$  models predict a softening behavior of Cu-0 at H1. In contrast, the  $\beta_1$ -model predicts a slowly hardening response. The reason for this softening behavior is the formation of intense shear bands in the Cu-0 matrix, as shown by the distribution of shear strain component  $\epsilon_{23}$  predicted by PH1- $\beta$  and PH1 Mosaic in Fig. 12(a) and Fig. 12(b), respectively. The observed localization bands tend to avoid the stiff Nb fibers. The highest strain localization (local shear strain up to  $\sim 15\%$  and  $\sim 10\%$  for PH1- $\beta$  and PH1 Mosaic respectively) occurs at the intersection points of localization bands and Nb fibers. According to Idiart et al. (2006), this phenomenon is often observed in full-field model responses due to the localization of strain field into bands running through the composite, along certain preferred orientations

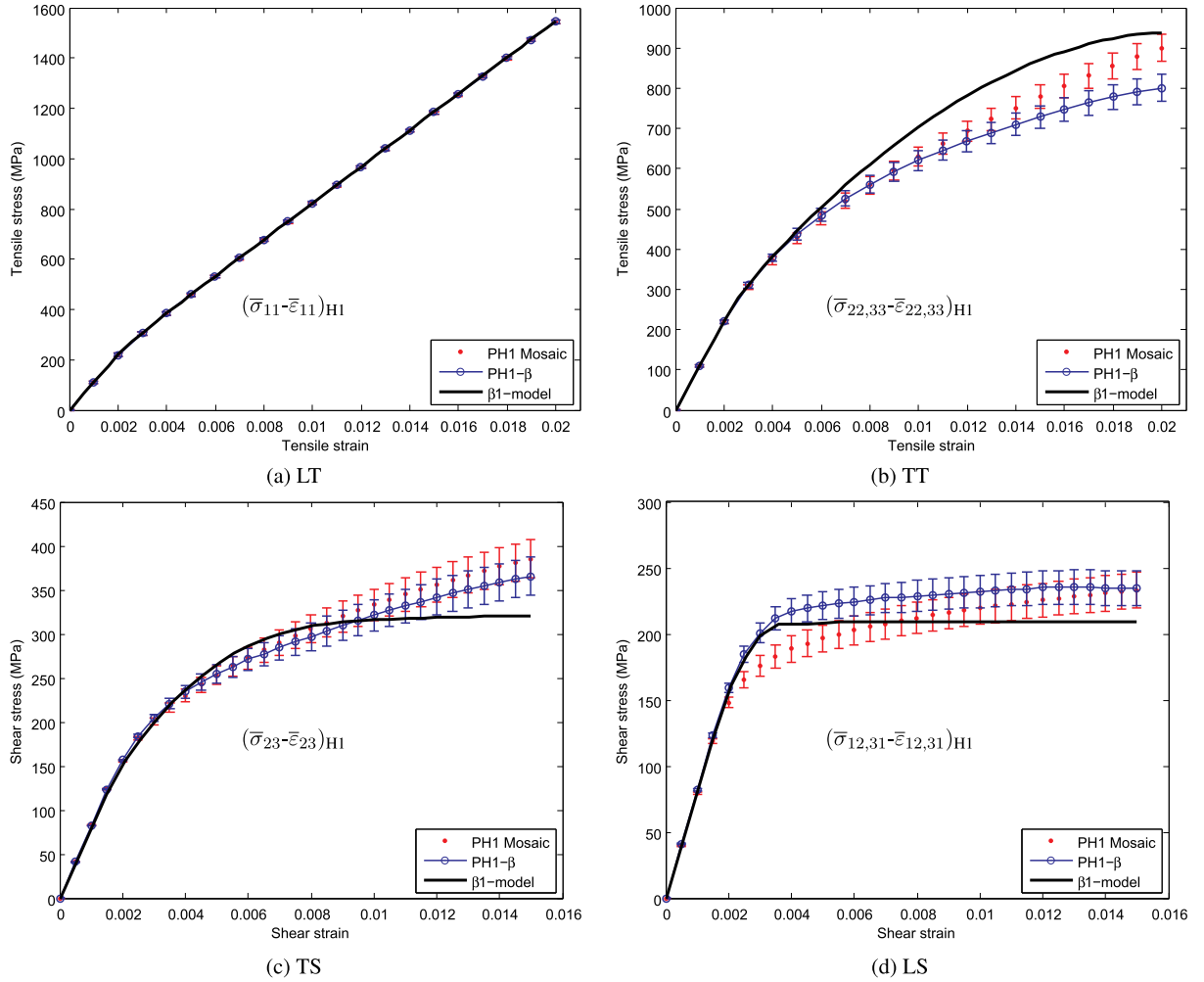


**Fig. 10.** Effective elasto-plastic behavior at scale H1, obtained by the PH1 Mosaic, PH1- $\beta$ , and  $\beta$ 1-model. Various loading conditions are presented: (a) LT, (b) TT, (c) TS and (d) LS tests.

determined by the loading conditions. Moreover, note that the homogeneous  $\beta$ 0-model in PH1- $\beta$  leads to a stronger strain localization and a softer plastic behavior, compared with the heterogeneous tessellation of PH1 Mosaic. This is due to the fact that grain boundaries represent obstacle to the shear band propagation, such grain boundaries being absent in the  $\beta$ 0-model in PH1- $\beta$ . In addition, we have also verified that higher mesh density will also lead to a stronger strain localization, without changing the constitutive law of pure copper. Similar strain localization phenomena also occurs for TT and LS tests. In contrast, this phenomenon is rather negligible in LT test due to the uniform longitudinal strain prescribed in Cu and Nb.

On the other hand, the responses of mean-field  $\beta$ 1-model does not display a softening at H1, as strain localization only occurs in full-field models. As explained in Section 4.3, the  $\beta$ -models tend to overestimate hardening due to the model assumptions. Mean field homogenization models are not designed for capturing localization effects. Furthermore, disregarding the hexagonal fiber assembly morphology at H1 in the  $\beta$ -models is believed to be another factor contributing to the model response deviations.

### 5.3. Iterative scale transition process up to H2

At scale H2, we suppose that 85 continuum cylinders are composed of two distinct zones: (1) the effective Cu-Nb composite zones containing 85<sup>1</sup> elementary long fibers (i.e. H1 zone); (2) the embedding matrix Cu-1. At this scale, the full-field PH2- $\beta$  and mean-field  $\beta$ 2-models are introduced. It has been proved previously that the  $\beta$ 1-model and  $\beta$ 0-model predict reliably the elasto-plastic behavior of H1 zone and polycrystalline Cu, respectively. Thus, the PH2- $\beta$  model takes these  $\beta$ -models as the local constitutive behavior of H1 zone and Cu-1. In addition, a three-phase (i.e. Nb, Cu-0 and Cu-1)  $\beta$ 2-model can also be defined to predict the elasto-plasticity at H2 without considering anymore the specific architecture.

The results of both models are reported here. The effective behavior and the average “local” behavior of each individual component are plotted in Fig. 13 and Fig. 14, respectively. In the captions, homogenization of the individual H1 zone and Cu-1 at H2 are

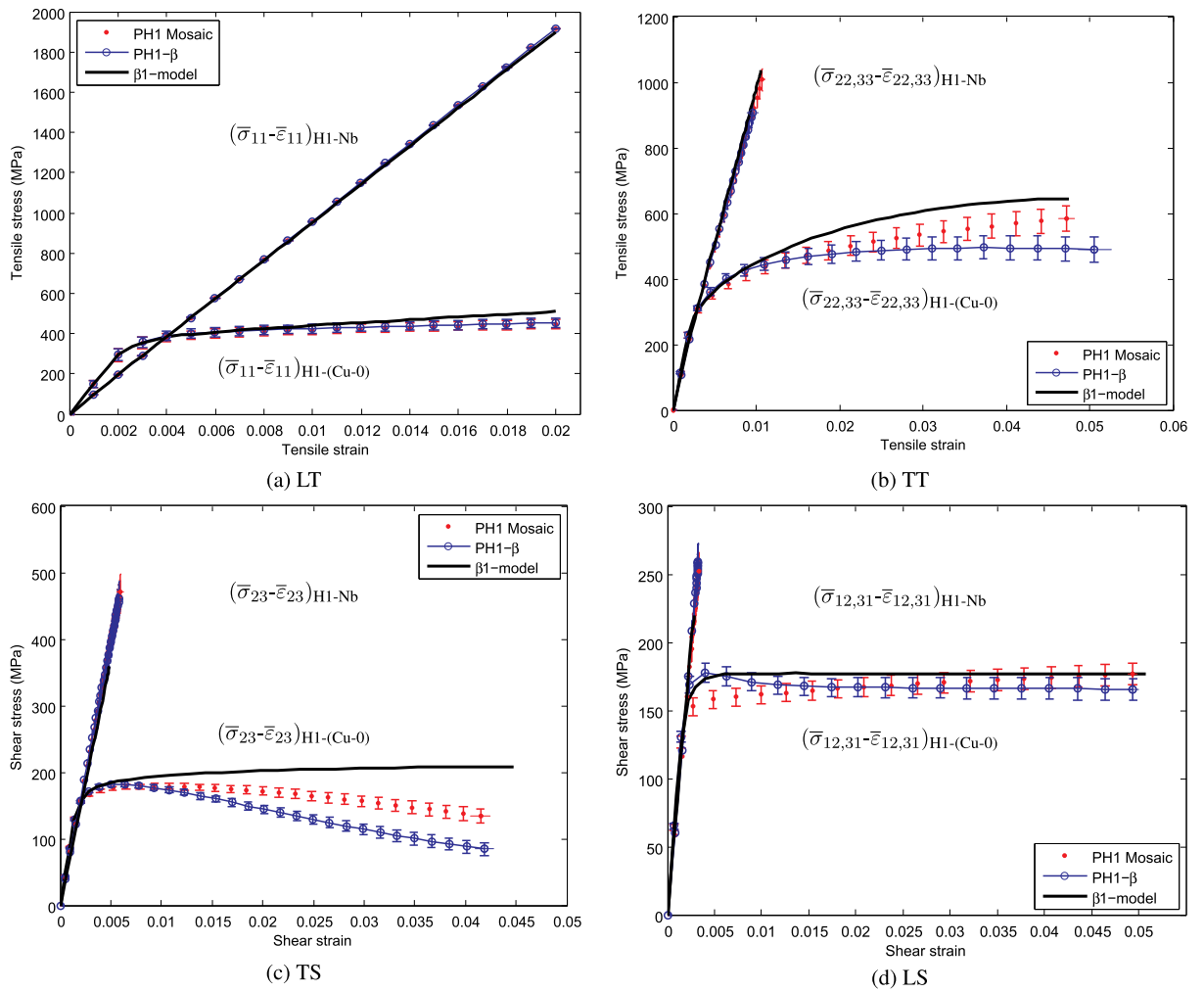


**Fig. 11.** Effective behavior of the individual Cu-0 and Nb components at scale H1, obtained by the PH1 Mosaic, PH1- $\beta$ , and  $\beta$ 1-model approaches. Various loading conditions are presented: (a) LT, (b) TT, (c) TS and (d) LS tests.

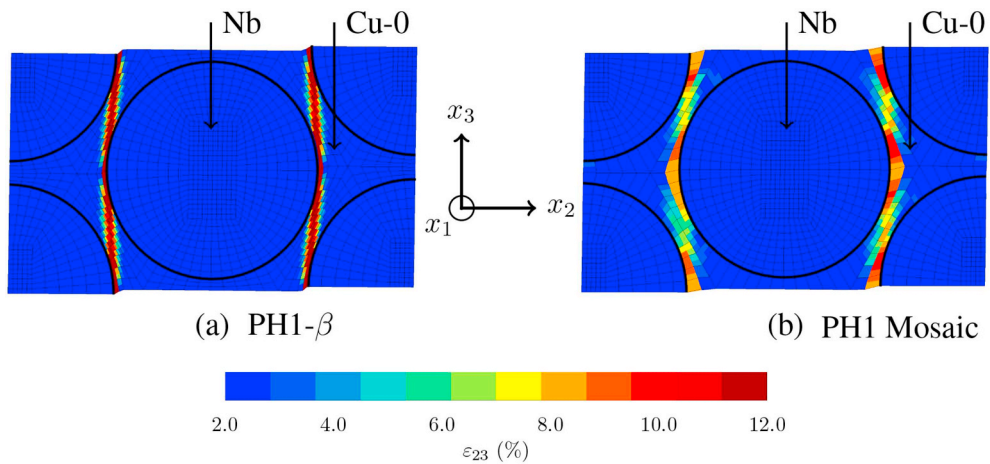


**Fig. 12.** Shear strain  $\varepsilon_{23}$  distribution predicted by the (a) PH1- $\beta$  and (b) PH1 Mosaic models at scale H1 with an overall effective transverse shear  $(\varepsilon_{23})_{H1} = 1.5\%$  imposed in the TS test.

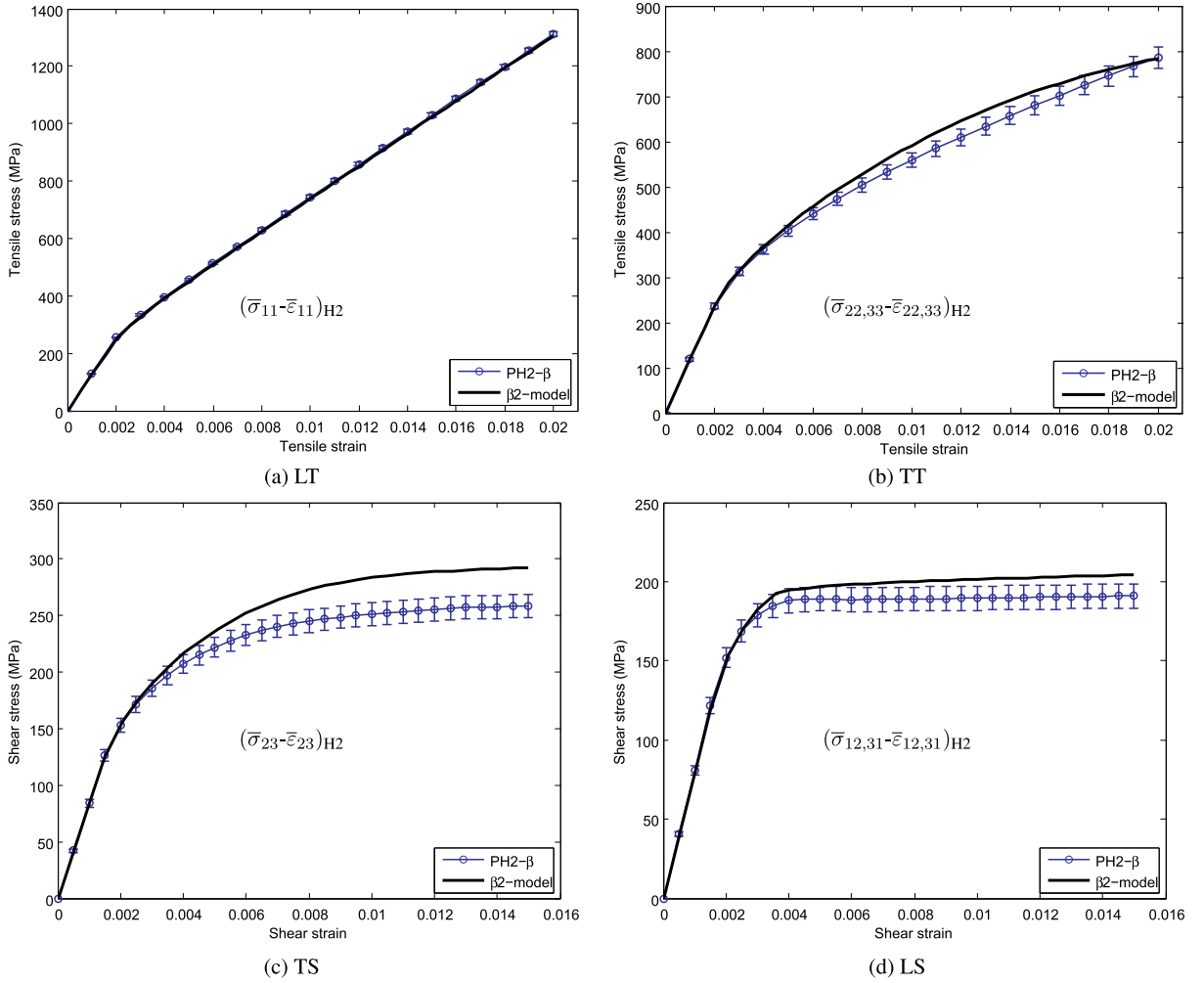


**Fig. 13.** Effective elasto-plastic behavior at scale H2, obtained by the PH2- $\beta$  and  $\beta$ 2-model for various loading conditions: (a) LT, (b) TT, (c) TS and (d) LS tests.

denoted H2-(H1 zone) and H2-(Cu-1), respectively. It is found that the full-field and mean-field methods provide close results at H2. The differences do not exceed  $\sim 15\%$ , reached for some loading conditions like TS. The main reasons for such deviation are believed to be the same as those discussed in Section 5.2 at H1, namely: (1) strain localization in the matrix; (2) absence of specific account of the architecture according to the  $\beta$ 2-model. In LT, the effective longitudinal Young's modulus and tangent modulus at H2 take the values  $\sim 124$  GPa (118 GPa in the H1 zone and 162 GPa in Cu-1) and  $\sim 57$  GPa respectively. Similar to the model responses at H1, for LT at H2, the imposed longitudinal strain is still uniform, i.e.  $(\bar{\epsilon}_{11})_{H2} = (\bar{\epsilon}_{11})_{H2-(H1\ zone)} = (\bar{\epsilon}_{11})_{H2-(Cu-1)}$ . In contrast, for TT, TS and LS, the average strains of H1 zone and Cu-1 matrix along loading conditions are  $\sim 1\%$  and  $\sim 3\%$  respectively, at the ultimate loading step.

#### 5.4. Error propagation and discussion about the best-suited modeling strategy

In this work, three homogenization models were applied to perform the scale transitions up to H1/H2. The  $\beta$ 1-model/ $\beta$ 2-model essentially assume a random mixture of Cu and Nb phases, whereas the PH1 Mosaic, PH1- $\beta$  (or PH2- $\beta$ ) models both take into account the hexagonal fiber assemblies with periodic distribution. These models provide close results (differences  $< \sim 15\%$ ) at scales H1/H2, in spite of the very different approximations of geometry.

Furthermore, error propagation needs to be discussed for hierarchical multiscale modeling, as the uncertainties will be accumulated by scale transition steps (Choi et al., 2008; McDowell, 2010). According to Choi et al. (2008), the types of uncertainty are categorized as follows:

- Natural uncertainty: uncertainty due to the inherent randomness or unpredictability of a physical system. Natural uncertainty related to the statistical RVE size has been estimated in Section 3.4 for all the models considered in this work.
- Model parameter uncertainty: incomplete knowledge of model parameters/inputs due to insufficient or inaccurate data. Model

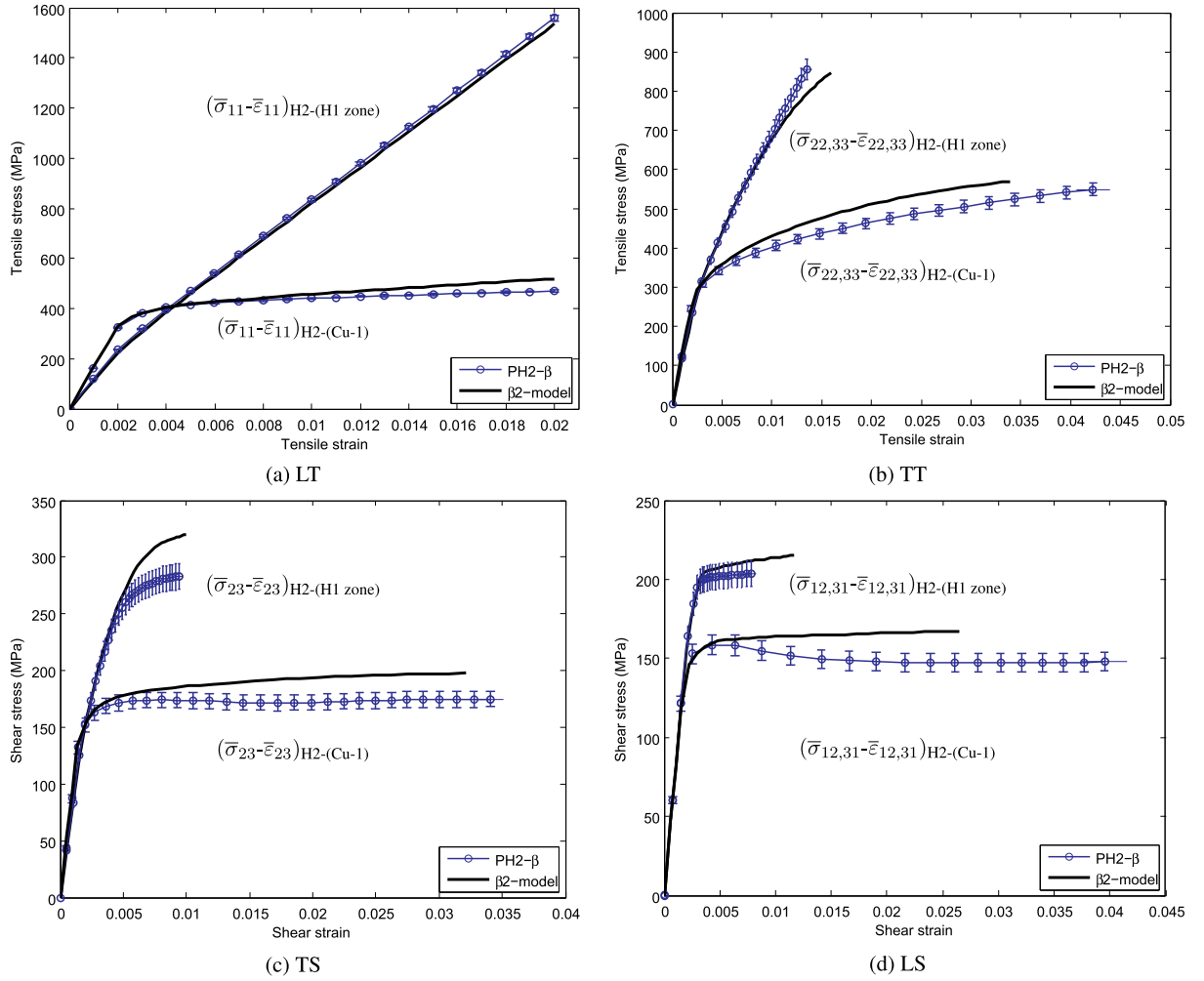


**Fig. 14.** Effective behavior of the individual H1 zones and Cu-1 components at scale H2, obtained by the PH2- $\beta$  and  $\beta$ 2-model for various loading conditions: (a) LT, (b) TT, (c) TS and (d) LS tests.

uncertainties here are mainly associated with crystallographic/morphological textures, initial residual stresses, parameters for single crystal plasticity and phenomenological  $\underline{\underline{D}}$  of the  $\beta$ -models. The textures used in this work are provided by EBSD data which was carefully measured at all scales in Cu-Nb specimens (see Section 2.2). Initial residual stresses in this work are identified by the comparison between model responses at scale S2 and tensile test data of Cu-Nb wires, this will be shown later in Section 6.2. The crystal plasticity parameters used in FEM for polycrystals are found to fit well for the elasto-plastic behavior of pure Cu (Section 4.1). This is however probably one way of improvement of the approach, since identification was limited to a tensile test and most parameters were taken from literature. Finally, the tensor  $\underline{\underline{D}}$  of the  $\beta$ -models was identified based on their full-field benchmarks in Section 4.3.

- **Model structure uncertainty:** uncertain model formulation due to approximations and simplifications. In particular, the full-field models were shown to be prone to shear localization, whereas the  $\beta$ -models cannot capture this phenomenon (Sections 5.2 and 5.3).
- **Propagated uncertainty:** this is an uncertainty expanded by a combination of the above three types of uncertainty in a chain of multiscale models. The interplay between architectures in the hierarchy is found to be lost in the proposed  $\beta$ -models.

It is worth noting that, for the practical application to Cu-Nb wires for winding coils, only the *longitudinal* mechanical properties are used in the design. As observed previously, the LT tests at all scales display only small uncertainties <5%, which makes the proposed models accurate enough and suitable for the application.

Finally, the computational efficiency must be considered for selecting the best-suited multi-scale modeling strategy. At scale H0, the computational time ratio is on the order of 1: 100 between the mean-field  $\beta$ 0-model and the full-field FEM for polycrystals. Moreover, at scale H1, this ratio becomes  $\sim$  1: 100: 1000 for the  $\beta$ 1-model, PH1 Mosaic and PH1- $\beta$  respectively. The simulation of the TS test, for instance, by means of these three models have taken *about 40 min, 3 days and 1 month* respectively, using the processors

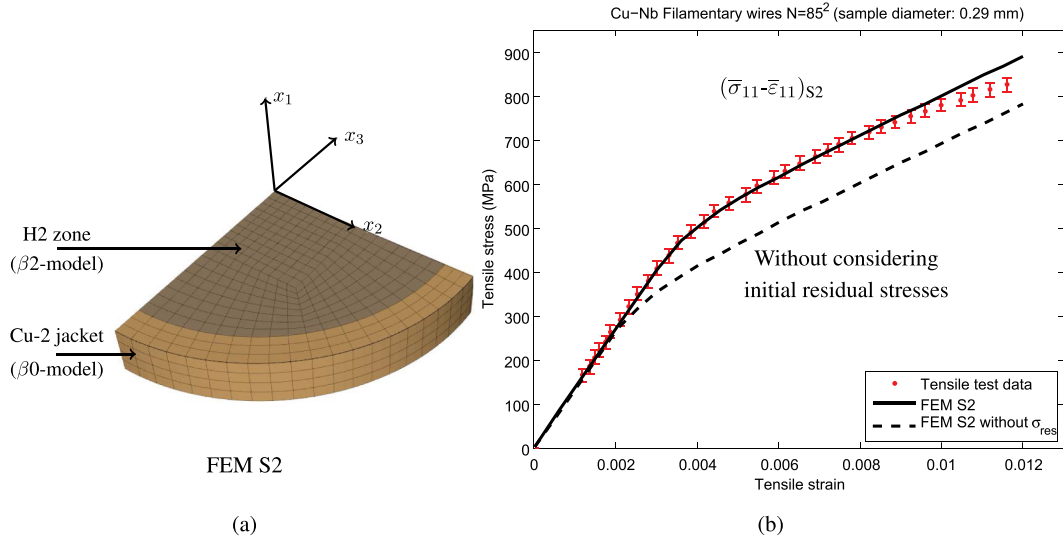


**Fig. 15.** (a) 1/4th FEM mesh of a cross-section of the S2 sample (the 3 elements in thickness are for illustration purposes since results are invariant along the wire length, i.e. cross-section thickness); (b) Experimental comparison for the monotonic LT test at S2. The dashed line in (b) shows the model prediction without taking into account the initial residual stresses.

Intel® Core™ i7-6600U (Dual Core, 2.6GHz, 4M cache, 15 W). It can be concluded that the  $\beta$ -models can be regarded as the best-suited models for Cu-Nb wires, with a good compromise in predictive capability and computational efficiency.

## 6. Comparison with experiments

The predictions of the previous multiscale models are now validated using experimental data. The macroscopic response of the structural problem S2 is compared to monotonic tensile test data in 6.1. Initial residual stresses are found to play an important role, particularly on the effective yield stress. This is discussed in Section 6.2. Section 6.3 briefly describes the in-situ neutron diffraction tensile experiments, carried out by Medy (2016). Section 6.4 demonstrates the predictive capability of our models for the in-situ data. It also provides a quantitative understanding of the lattice strain evolution during uniaxial loading test in the multiscale nanocomposite.

### 6.1. Structural problem S2 and comparison with macroscopic tensile test

As illustrated in Fig. 1(c) and detailed in Section 2.3, a real Cu-Nb wire can be seen as a single cylinder-shaped structure at macro-scale (i.e. S2). Fig. 15(a) indicates 1/4th of the S2 sample cross-section with the corresponding finite element mesh. In this model, the local properties of the inner Cu-Nb composite H2 zone and the external polycrystalline Cu-2 jacket are assigned to the  $\beta_2$ -model (Section 5.3) and the  $\beta_0$ -model for H0-(Cu-2) (Section 4) respectively. In order to save CPU time, symmetric boundary conditions are applied:  $U_2$  and  $U_3$  (displacement field along  $x_2$  and  $x_3$ ) are fixed to zero at the vertical planes  $x_2 = 0$  and  $x_3 = 0$  respectively. A normal displacement is prescribed to the two terminal sections of this S2 specimen. These sections are assumed to remain flat. From the computed axial force, the effective behavior of S2 is obtained, as illustrated by the dashed curve in Fig. 15(b).

Due to the high resistance of Cu-Nb wires (Thilly et al., 2002), slip between the specimen and the grips was often observed during tensile tests, leading to a difficulty in strain measurement for the macroscopic tensile curves recorded during in-situ diffraction tests (Vidal, 2006). Therefore, an complementary ex-situ monotonic tensile test along  $x_1$  was carried out. In order to determine the strain along  $x_1$  with sufficient accuracy, DIC (Digital Image Correlation) was used for Cu-Nb wires, as for the pure copper wires described in section 4.1. The points in Fig. 15(b) refer to the experimental results. The macroscopic longitudinal Young's modulus  $E_1$  and yield stress  $\sigma_y$  along the wire direction  $x_1$  are found respectively to be  $\sim 140$  GPa and  $\sim 650$  MPa (according to the criterion for macro-yield stress at a tangent modulus equaling to one third of the elastic modulus following Thilly et al. (2009)). The model results without considering initial residual stresses are compared with experimental data in Fig. 15(b). It is found that they display very similar elastic modulus and plastic hardening, however the effective yield stresses significantly differ. This comparison leads to a critical assessment of the initial approach and raises the question of existence of residual stresses originating from material processing. These initial stresses are identified in the next subsection.

### 6.2. Identification of initial residual stresses

Both initial residual stresses  $\sigma_{res}$  and yield stress of polycrystalline Cu component  $\sigma_y^{Cu}$  determine the apparent yield stress of Cu-Nb wires, as shown in Fig. 15(b). However, the exact values of  $\sigma_{res}$  are not known yet for the Cu-Nb Filamentary wires  $N = 85^2$  studied in

**Table 4**

Initial residual stresses and eigenstrains used in the individual polycrystalline Cu/Nb components. These values are chosen in such a way that model results fit the data of macroscopic LT test. Signs +/− indicate that Nb and Cu components are in axial tension and compression respectively. In this work, the two Cu-Nb composite samples with different diameters are assumed to exhibit the same initial residual stresses and eigenstrains in each component.

Component	Nb	Cu-i (i = 0,1,2)
$(\sigma_{\text{res}})_{11}$	+250 MPa	−200 MPa
$(\varepsilon_0)_{11}$	−0.26%	0.12%
$(\varepsilon_0)_{22,33}$	0.104%	−0.040%

this work. Instead,  $(\sigma_{\text{res}})_{11}$  of Nb is chosen to be +250 MPa in tension which is assumed to be equal to the one in  $N = 55^4$  type of Cu-Nb wires, as measured by X-ray diffraction by Vidal (2006). To ensure macroscopic equilibrium of the whole Cu-Nb wires, i.e.  $(\bar{\sigma}_{\text{res}})_{S2} = 0$ ,  $(\sigma_{\text{res}})_{11}$  is determined as -200 MPa in compression for Cu components.  $\sigma_{\text{res}}$  in transverse directions and in shear directions are assumed to be zero, due to lack of data. It will be shown that this approximation is sufficient to predict the longitudinal elasto-plastic behavior of Cu-Nb wires based on the available mechanical data.

Initial residual stresses  $\sigma_{\text{res}}$ , are usually generated by appropriate eigenstrains  $\varepsilon_0$  (called also “stress-free strains”) in each component, based on the thermo-elastic like homogenization problems, e.g. Masson et al. (2000); Brenner et al. (2004). For the detailed derivations, refer to Appendix A.1. In the present work,  $\varepsilon_0$  is identified in such a way that the generated stress  $\sigma_{\text{res}}$  takes the required value. All the related non-zero components in  $\sigma_{\text{res}}$  and  $\varepsilon_0$  are reported in Table 4. The eigenstrain prescribed in Nb components,  $(\varepsilon_0)_{11}$ , takes a negative value. Due to the interaction between Nb and Cu (i.e. equilibrium of the composite), Nb will be in axial tension with positive  $(\sigma_{\text{res}})_{11}$ . Similarly,  $(\varepsilon_0)_{11}$  of Cu takes a positive value. With these values of  $\sigma_{\text{res}}$ , the model responses at S2 display a good agreement with the tensile test data, as shown by Fig. 15(b). By comparing the dashed and solid stress-strain curves (without vs. with  $\sigma_{\text{res}}$  accounted for), the impact of residual stresses is found to be as large as  $\sim 100$  MPa.

Some arguments in Medy (2016) suggest that  $(\sigma_{\text{res}})_{11}$  in large Cu channels may not be as high as −200 MPa, estimated by preliminary neutron diffraction tests. Therefore, an axial compression value of -100 MPa for Cu components is also used. In this case, a tension of +125 MPa for Nb is determined to fulfill a zero  $(\bar{\sigma}_{\text{res}})_{S2}$ . It is found that, if the yield stress value is modified to  $\sigma_y^{\text{Cu}} = 450$  MPa, the homogenization at S2 still predicts the same tensile results. This confirms the empirical formula proposed in Vidal et al. (2009): the sum of  $\sigma_y^{\text{Cu}}$  and  $|(\sigma_{\text{res}}^{\text{Cu}})_{11}|$  equal to a constant for Cu-Nb wires, here  $\sigma_y^{\text{Cu}} + |(\sigma_{\text{res}}^{\text{Cu}})_{11}| \approx 550$  MPa. Thus, there still exists various possible combinations of  $(\sigma_{\text{res}})_{11}^{\text{Cu}}$  and  $\sigma_y^{\text{Cu}}$ . Further X-ray/neutron diffraction experiments are in preparation for investigating  $(\sigma_{\text{res}})_{11}$  of both Cu and Nb precisely. The  $\sigma_{\text{res}}$  and  $\sigma_y^{\text{Cu}}$  proposed respectively in Table 4 and 2 are used throughout this work.

### 6.3. In-situ neutron diffraction tensile experiments

Besides the macroscopic tensile tests, an in-situ neutron diffraction tensile experiment was performed by Medy (2016) on the Cu-Nb Filamentary wires  $N = 85^2$  at 6T1 diffractometer of Orphée-LLB (CEA Saclay, France). The sample diameter, applied strain rate and temperature were 2.10 mm,  $10^{-5} \text{ s}^{-1}$  and 293 K respectively. The detailed information on the setup can be found in Medy (2016).

By analyzing the shift of  $\{hkl\}$  Bragg peaks, neutron diffraction provides information about the incremental mean elastic strain within the diffracting volume. Diffraction volume is constituted by all grains fulfilling Bragg conditions, i.e. exhibiting an  $\{hkl\}$  plane perpendicular to diffraction vector  $\mathbf{G}$ . Medy (2016) took advantage of the strong crystallographic texture of the specimen for the analysis: for Cu, the double  $\langle 100 \rangle$  and  $\langle 111 \rangle$  fibers lead to respectively a significant proportion of  $\{200\}$  and  $\{111\}$  planes perpendicular to the wire axis  $x_1$ ; similarly for Nb, the strong  $\langle 110 \rangle$  fibers lead to  $\{220\}$  planes perpendicular to  $x_1$ . Taking the diffraction vector  $\mathbf{G}/x_1$  and performing diffraction on these lattice planes allows estimating the incremental longitudinal mean elastic strain, i.e.  $\Delta(\varepsilon_e^{\langle 111 \rangle \text{Cu}})_L$ ,  $\Delta(\varepsilon_e^{\langle 100 \rangle \text{Cu}})_L$  and  $\Delta(\varepsilon_e^{\langle 110 \rangle \text{Nb}})_L$ , within the corresponding diffraction volumes, for individual  $\langle 111 \rangle$  Cu,  $\langle 100 \rangle$  Cu and  $\langle 110 \rangle$  Nb fibers respectively. The incremental elastic strain is defined as  $\Delta\varepsilon_e = \varepsilon_e - \varepsilon_e(t < 0)$  where  $\varepsilon_e(t < 0)$  indicates the elastic strain before loading. The presence of initial residual stresses leads to  $\varepsilon_e(t < 0) \neq 0$  for Cu-Nb wires (refer to A.1). However, the absolute experimental values of  $\varepsilon_e(t < 0)$  remain unknown, only the incremental values  $\Delta\varepsilon_e$  are reported in Medy (2016). Measurements of absolute strains require complex calibration of reference lattice spacing, not tackled in the present work.

Fig. 16 shows the lattice strain evolution of the individual fiber texture components in terms of the applied tensile stress  $(\bar{\sigma}_{11})_{S2}$ . The fitting of Bragg peak position leads to an uncertainty of  $\sim \pm 0.05\%$  for determining  $(\varepsilon_e)_L$ . In addition, long exposure time in neutron diffraction experiments led to stress relaxation during the measurement. Therefore, an uncertainty of  $\pm 15$  MPa for the applied tensile stress  $(\bar{\sigma}_{11})_{S2}$  is associated.

### 6.4. Comparison with in-situ experiments

According to Upadhyay et al. (2016); Gu et al. (2017a), a comparison with diffraction data requires (1) to compute the mean stresses acting on H2 zone and Cu-2 as a function of tensile strain by FEM S2; (2) to compute the corresponding stress and strain concentration within the grains, by means of the  $\beta$ -models in H2 zone and Cu-2 separately; (3) to isolate the diffraction volume and

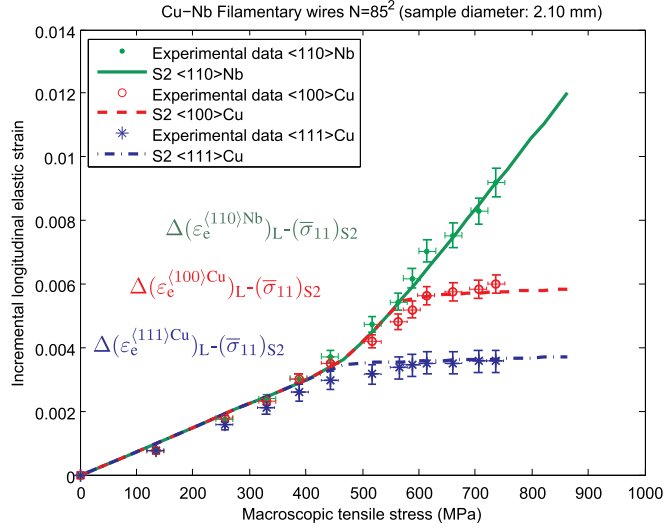


**Fig. 16.** Experimental comparison with the in-situ neutron diffraction tensile experiments (data obtained by Medy (2016)): applied macroscopic monotonic longitudinal stress  $(\bar{\sigma}_{11})_{S2}$  vs. incremental longitudinal mean elastic strains of individual  $\langle 111 \rangle$  Cu,  $\langle 100 \rangle$  Cu and  $\langle 110 \rangle$  Nb fiber textures, i.e.  $\Delta(\varepsilon_e^{(111)Cu})_L$ ,  $\Delta(\varepsilon_e^{(100)Cu})_L$  and  $\Delta(\varepsilon_e^{(110)Nb})_L$ .

calculate the mean elastic strain along the direction of diffraction vector  $\mathbf{G}$  in this volume; (4) to gather the mean incremental elastic strains for the individual fiber textures. The results obtained in that way are shown in Fig. 16, with an excellent match for all three analyzed components.

Based on Fig. 15 and 16, one can conclude that the proposed elasto-plastic models not only predict the correct effective behavior, but also provide a good estimation of the stress and strain distributions within Cu and Nb fiber components. Slight deviations between experiments and theory can still be observed, especially regarding the overestimated hardening after some strain level in Fig. 15 and overestimated yield in Cu components in Fig. 16. They can be attributed to the following reasons: (1) High density of micro-defects introduced in the fabrication process, particularly during the severe plastic deformation. These defects probably reduce the ductility of Cu-Nb wires, and lead the deviations between experimental data and model predictions, especially when the applied strain  $>1\%$ ; (2) model parameters of single crystal plasticity were fitted for the highly hardened pure Cu, instead of the actual polycrystalline Cu components in Cu-Nb wires; (3) simplifications within the  $\beta$ -models; (4) crystallographic textures used in models are obtained from the sample with a diameter of 4.50 mm, instead of the smaller samples for mechanical tests.

Furthermore, both experiments and theory show that the increasing of  $\Delta(\varepsilon_e^{(111)Cu})_L$  and  $\Delta(\varepsilon_e^{(100)Cu})_L$  saturate at 0.004 and 0.006 respectively, corresponding to  $(\bar{\sigma}_{11})_{S2} = 450$  MPa and 550 MPa. This means that plastic activity occurs in  $\langle 100 \rangle$  oriented grains at a higher macroscopic applied stress than in  $\langle 111 \rangle$  grains in tensile loading along the wire direction. A similar phenomenon was observed for pure Cu polycrystals at H0 in LT, as mentioned in Section 4.2. Based on Fig. 9(a), this is because  $\langle 100 \rangle$  oriented grains exhibit a lower stiffness and thus are subjected to a lower stress, and then reach their yield limit at a later stage despite their lower yield stress. On the other hand, the good agreement between experiments and theory confirms the assumption of elastic behavior for Nb. Larger stress levels are required to activate plasticity in Nb.

## 7. Conclusions

This work focuses on multiscale modeling of the elasto-plastic behavior of architected and nanostructured Cu-Nb composite wires. The main conclusions of the study are the following:

- (1) *Hierarchical homogenization strategy.* As the specimens exhibit several characteristic scales, an original iterative scale transition elasto-plastic homogenization approach was proposed considering the specific texture and architecture of Cu-Nb wires.
- (2) *Full field vs. mean field method.* In order to investigate the links between the effective material behavior and the wire micro-structure, full-field finite element homogenization was carried out at first. The mean-field  $\beta$ -models were then proposed to save computational time and appropriately calibrated to perform iterative scale transition steps. Reasonable agreement was found between the full-field and reduced order models at all the considered scales.
- (3) *Model responses vs. data of macroscopic tensile test and in-situ test.* Mechanical modeling was experimentally validated by both macroscopic tensile test and in-situ neutron diffraction test where the mean elastic strains were measured in the individual copper and niobium texture components.
- (4) *Initial residual stresses* were to be taken into account in order to reach agreement between model and experiments. They are related to material processing of the Cu-Nb wires.
- (5) *Plastic activity in different Cu/Nb texture components.* In Cu-Nb wires, polycrystalline Cu exhibits a double  $\langle 100 \rangle$ – $\langle 111 \rangle$  fiber texture.

Experiments and theory show consistently that plastic activity occurs in  $\langle 100 \rangle$  oriented grains at a higher applied macroscopic stress than in  $\langle 111 \rangle$  grains in tensile loading along the wire direction.

Only tensile tests can be performed in-situ with such thin wires. Here, several in-situ tensile tests have been performed for each type of wire and provide the same results with respect to the evolution of lattice strain evolution with respect to applied stress. The experimental error on lattice strain values is estimated to be smaller than 4% in such tests so that the good agreement between experimental and simulation results is already a great achievement, in favor of the accuracy of the proposed model. Further work is in progress in the following directions:

- (1) Even though *grain size effect* has been taken into account in this work for Cu-Nb Filamentary wires  $N = 85^2$ , its impact on effective material behavior is not significant, as the volume fraction of fine Cu components is rather small ( $\sim 15\%$ ). In contrast, other types of Cu-Nb wires, such as the Filamentary wires  $N = 85^3$  (see Gu et al. (2017b) for the material descriptions), exhibit a higher volume fraction of ultra-fine Cu grains. The importance of size effects will be studied by multiscale modeling for these Cu-Nb wires.
- (2) Careful measurements of *residual stresses* are still needed by X-ray or neutron diffraction for the Cu-Nb wires studied in this work. In addition, simulation of material processing could also help determining quantitatively the residual stresses but this remains a very demanding task involving grain fragmentation and recrystallization.
- (3) *Various loading conditions*, such as the TT test or torsion, can be performed by ex-situ or in-situ experiments. Such additional complex tests are necessary to validate the full elasto-plastic multi-scale modeling approach. Finally, cyclic tensile tests were also performed for Cu-Nb wires by Thilly et al. (2009). Significant “Bauschinger effect” was observed, demonstrating strong kinematic hardening. The model can also be used for comparisons with this data.

Finally, the theoretical models will be used to optimize the microstructure parameters in the fabrication process of Cu-Nb wires.

## Acknowledgments

The authors gratefully acknowledge the support provided by ANR through the METAFORES ANR-12-BS09-0002 project. Tang Gu wishes to thank Florent Coudon (Safran Tech & Mines ParisTech) for his help in  $\beta$ -model derivations and codes. T.G. also thanks Jean-Christophe Teissedre, Julie Heurtel and Anne Laurent (Mines ParisTech) for their help in performing ex-situ tensile tests and complementary EBSD experiments. Florence Lecouturier wishes to thank Nelson Ferreira (LNCMi-Toulouse) for the drawing of Cu-Nb wires.

## Appendix A. Derivation of mean-field $\beta$ -model

### Appendix A.1. Thermo-elastic standard self-consistent scheme

In polycrystals, the local elastic stiffness tensor  $\underline{\underline{\mathbb{C}}}(\mathbf{x})$  is a uniform property inside the grains. The quantity  $\underline{\underline{\mathbb{C}}}(\mathbf{x})$  can therefore be replaced by the corresponding homogeneous values  $\underline{\underline{\mathbb{C}}}^{(r)}$  of the considered mechanical phase ( $r$ ). Local and effective thermo-elastic constitutive relations write respectively:

$$\underline{\underline{\sigma}}^{(r)} = \underline{\underline{\mathbb{C}}}^{(r)} : (\underline{\underline{\varepsilon}}^{(r)} - \underline{\underline{\varepsilon}}_0^{(r)}), \quad \underline{\underline{\sigma}} = \underline{\underline{\mathbb{C}}} : (\underline{\underline{\varepsilon}} - \underline{\underline{\varepsilon}}_0) \quad (\text{A.1})$$

where  $\langle \cdot \rangle^{(r)}$  indicates the average over the volume of phase ( $r$ ), e.g.  $\underline{\underline{\varepsilon}}^{(r)} = \langle \underline{\underline{\varepsilon}}(\mathbf{x}) \rangle_{(r)}$ . In addition,  $\underline{\underline{\varepsilon}}_0^{(r)}$  denotes a uniform eigenstrain associated with temperature changes in thermo-elasticity. In this work,  $\underline{\underline{\varepsilon}}_0^{(r)}$  are initially implemented in composite Cu-Nb wires to generate the residual stresses. According to e.g. Masson et al. (2000); Castelnau (2011), it can be shown that the effective elastic tensor  $\underline{\underline{\mathbb{C}}}$  and the effective stress-free strain  $\underline{\underline{\varepsilon}}_0$  read:

$$\underline{\underline{\mathbb{C}}}^{-1} = \langle \underline{\underline{\mathbb{C}}}^{(r)-1} : \underline{\underline{\mathbb{B}}}^{(r)} \rangle, \quad \underline{\underline{\varepsilon}}_0 = \langle \underline{\underline{\varepsilon}}_0^{(r)} : \underline{\underline{\mathbb{B}}}^{(r)} \rangle \quad (\text{A.2})$$

where  $\underline{\underline{\mathbb{B}}}^{(r)}$  denotes the stress concentration tensor determined by the pure elastic SSC scheme. In addition, according to the definition of  $\underline{\underline{\mathbb{B}}}^{(r)}$ ,  $\underline{\underline{\sigma}}^{(r)}$  can be expressed as:

$$\underline{\underline{\sigma}}^{(r)} = \underline{\underline{\mathbb{B}}}^{(r)} : \underline{\underline{\sigma}} + \underline{\underline{\sigma}}_{\text{res}}^{(r)} \quad (\text{A.3})$$

with  $\underline{\underline{\sigma}}$  and  $\underline{\underline{\sigma}}_{\text{res}}^{(r)}$  being respectively the macroscopic applied stress and initial residual stresses in phase ( $r$ ). To estimate the phase-average stress and strain, phase ( $r$ ) is treated according to the SSC scheme as an ellipsoidal inclusion embedded in an HEM (Homogeneous Equivalent Medium) whose behavior represents that of the polycrystal. Eshelby's inclusion formalism (Eshelby, 1957) is used to describe the interaction between each phase and the aggregate. According to e.g. (François et al., 1998; Qu and Cherkouhi, 2006; Nemat-Nasser and Hori, 2013),  $\underline{\underline{\mathbb{B}}}^{(r)}$  is derived as:

$$\underline{\underline{\mathbb{B}}}^{(r)} = \underline{\underline{\mathbb{C}}}^{(r)} : \left[ \underline{\underline{\mathbb{I}}} + \underline{\underline{\mathbb{S}}}_{\text{Esh}} : \underline{\underline{\mathbb{C}}}^{-1} : \left( \underline{\underline{\mathbb{C}}}^{(r)} - \underline{\underline{\mathbb{C}}} \right) \right]^{-1} : \underline{\underline{\mathbb{C}}}^{-1} \quad (\text{A.4})$$

with  $\underline{\underline{I}}$  the fourth order identity tensor and  $\underline{\underline{S}}_{\text{Esh}}$  the Eshelby tensor. In addition,  $\underline{\underline{S}}_{\text{Esh}}$  is calculated as function of  $\underline{\underline{C}}$  and aspect ratio  $\ell/d$  for a spheroidal inclusion after (Mura, 1987; Suvorov and Dvorak, 2002). If the considered volume is a RVE, one gets:

$$\langle \underline{\underline{B}}^{(r)} \rangle = \underline{\underline{I}}. \quad (\text{A.5})$$

Before loading (i.e.  $t < 0$ ), the macroscopic stress  $\bar{\sigma} = \mathbf{0}$  to ensure equilibrium. This leads to  $\bar{\varepsilon} = \tilde{\varepsilon}_0$  and  $\sigma^{(r)} = \sigma_{\text{res}}^{(r)}$  by using Equations (A.1) and (A.3) respectively. Furthermore,  $\sigma_{\text{res}}^{(r)}$  can be written as follows based on the interaction equation of the pure elastic SSC before loading (Brenner et al., 2004):

$$\sigma_{\text{res}}^{(r)} = \left( \underline{\underline{C}}^{(r-1)} + \underline{\underline{C}}^{*-1} \right)^{-1} : \left( \tilde{\varepsilon}_0 - \varepsilon_0^{(r)} \right) \quad (\text{A.6})$$

where the effective stress-free strain  $\tilde{\varepsilon}_0$  is given in Eq. (A.2). The ‘‘Hill constraint tensor’’  $\underline{\underline{C}}^*$  is given by

$$\underline{\underline{C}}^* = \underline{\underline{C}} : \left( \underline{\underline{S}}_{\text{Esh}}^{-1} - \underline{\underline{I}} \right). \quad (\text{A.7})$$

At  $t < 0$ , it is worth noting that  $\varepsilon^{(r)} \neq \varepsilon_0^{(r)}$ . Based on Eq. (A.1):

$$\varepsilon^{(r)} = \underline{\underline{C}}^{(r-1)} : \sigma_{\text{res}}^{(r)} + \varepsilon_0^{(r)} \quad (\text{A.8})$$

where  $\sigma_{\text{res}}^{(r)}$  can be calculated in Eq. (A.6). Thus before loading, local strain  $\varepsilon^{(r)}$  is the sum of the stress-free strain  $\varepsilon_0^{(r)}$  and an elastic part  $\underline{\underline{C}}^{(r-1)} : \sigma_{\text{res}}^{(r)}$  necessary to ensure stress equilibrium.

#### Appendix A.2. Hill's elasto-plastic homogenization model

Hill (1965); Turner and Tomé (1994) introduced an incremental self-consistent homogenization model for the elasto-plastic behavior of polycrystalline aggregates. The linearized local and effective rate-independent constitutive relations are written respectively:

$$\dot{\sigma}^{(r)} = \underline{\underline{L}}^{(r)} : \dot{\varepsilon}^{(r)}, \quad \dot{\sigma} = \underline{\underline{L}} : \dot{\varepsilon} \quad (\text{A.9})$$

where  $\dot{\sigma}$  and  $\dot{\varepsilon}$  are the stress and strain rate tensors and  $\underline{\underline{L}}$  the tensor of tangent elasto-plastic moduli. Similarly to the elastic SSC scheme, in Hill's model, stress equilibrium is solved for one phase embedded in the HEM using the Eshelby formalism. The stress rate and strain rate are related through the following interaction equation:

$$\begin{cases} \dot{\sigma} - \dot{\sigma}^{(r)} = -\underline{\underline{L}}^* : (\dot{\varepsilon} - \dot{\varepsilon}^{(r)}), \\ \underline{\underline{L}}^* = \underline{\underline{L}} : \left( \underline{\underline{S}}_{\text{Esh}}^{-1} - \underline{\underline{I}} \right). \end{cases} \quad (\text{A.10})$$

It is worth noting that the Eshelby tensor  $\underline{\underline{S}}_{\text{Esh}}$  is determined by the effective elasto-plastic instantaneous moduli  $\underline{\underline{L}}$  and  $\ell/d$ . In this elasto-plastic model,  $\varepsilon^{(r)}$  is decomposed into elastic part  $\varepsilon_e^{(r)}$  and plastic part  $\varepsilon_p^{(r)}$ . Thus, we can express  $\varepsilon^{(r)}$  and  $\sigma^{(r)}$  accounting for initial residual stresses

$$\varepsilon^{(r)} = \varepsilon_e^{(r)} + \varepsilon_p^{(r)}, \quad \sigma^{(r)} = \underline{\underline{C}}^{(r)} : \left( \varepsilon_e^{(r)} - \varepsilon_0^{(r)} \right) \quad (\text{A.11})$$

where the used Hooke law is equivalent to the local thermo-elastic constitutive relation in Eq. (A.1). In addition, at  $t < 0$ ,  $\varepsilon_p^{(r)} = \mathbf{0}$  and  $\sigma^{(r)} = \sigma_{\text{res}}^{(r)}$ , leading to  $\varepsilon^{(r)} = \varepsilon_e^{(r)} = \underline{\underline{C}}^{(r-1)} : \sigma_{\text{res}}^{(r)} + \varepsilon_0^{(r)}$  as in the elastic case, see Eq. (A.8).

The results derived in the following steps are valid for Hill's homogenization approach but they will also be used in the  $\beta$ -model described in section Appendix A.4 below. The effective strain is decomposed into a macroscopic elastic strain tensor  $\tilde{\varepsilon}_e$  ( $\neq \bar{\varepsilon}_e$ ) and a macroscopic plastic strain  $\tilde{\varepsilon}_p$  ( $\neq \bar{\varepsilon}_p$ ), i.e.

$$\tilde{\varepsilon} = \tilde{\varepsilon}_e + \tilde{\varepsilon}_p + \tilde{\varepsilon}_0, \quad \bar{\sigma} = \underline{\underline{C}} : \tilde{\varepsilon}_e. \quad (\text{A.12})$$

At  $t < 0$ , one has  $\bar{\sigma} = \mathbf{0}$ ,  $\tilde{\varepsilon}_e = \tilde{\varepsilon}_p = \mathbf{0}$  and  $\tilde{\varepsilon} = \tilde{\varepsilon}_0$  which is computed by means of Eq. (A.2). Then derivatives of the above two equations with respect to time give:

$$\begin{cases} \dot{\varepsilon}^{(r)} = \dot{\varepsilon}_e^{(r)} + \dot{\varepsilon}_p^{(r)}, & \left\{ \begin{array}{l} \dot{\varepsilon} = \dot{\varepsilon}_e + \dot{\varepsilon}_p, \\ \dot{\sigma}^{(r)} = \underline{\underline{C}}^{(r)} : \dot{\varepsilon}_e^{(r)}, \end{array} \right. & \left\{ \begin{array}{l} \dot{\varepsilon} = \dot{\varepsilon}_e + \dot{\varepsilon}_p, \\ \dot{\sigma} = \underline{\underline{C}} : \dot{\varepsilon}_e. \end{array} \right. \end{cases} \quad (\text{A.13})$$

Multiplying Eq. (A.10) by  $\underline{\underline{S}}_{\text{Esh}} : \underline{\underline{L}}^{-1}$  and then substituting Eq. (A.13) into Eq. (A.10):

$$\begin{aligned} \underline{\mathbf{S}}_{\text{Esh}} : \underline{\tilde{\mathbf{L}}}^{-1} : \dot{\boldsymbol{\epsilon}}^{(r)} &= \underline{\mathbf{S}}_{\text{Esh}} : \underline{\tilde{\mathbf{L}}}^{-1} : \dot{\boldsymbol{\epsilon}} + \left( \underline{\mathbf{I}} - \underline{\mathbf{S}}_{\text{Esh}} \right) : \left( \dot{\boldsymbol{\epsilon}} - \dot{\boldsymbol{\epsilon}}^{(r)} \right) \\ &= \underline{\mathbf{S}}_{\text{Esh}} : \underline{\tilde{\mathbf{L}}}^{-1} : \dot{\boldsymbol{\epsilon}} + \left( \underline{\mathbf{I}} - \underline{\mathbf{S}}_{\text{Esh}} \right) : \left( \underline{\tilde{\mathbf{C}}}^{-1} : \dot{\boldsymbol{\epsilon}} + \dot{\boldsymbol{\epsilon}}_{\text{p}} - \underline{\mathbf{C}}^{(r-1)} : \dot{\boldsymbol{\epsilon}}^{(r)} - \dot{\boldsymbol{\epsilon}}_{\text{p}}^{(r)} \right) \end{aligned}$$

from which the following relation is obtained:

$$\left[ \underline{\mathbf{S}}_{\text{Esh}} : \underline{\tilde{\mathbf{L}}}^{-1} + \left( \underline{\mathbf{I}} - \underline{\mathbf{S}}_{\text{Esh}} \right) : \underline{\tilde{\mathbf{C}}}^{(r-1)} \right] : \dot{\boldsymbol{\epsilon}}^{(r)} = \left[ \underline{\mathbf{S}}_{\text{Esh}} : \underline{\tilde{\mathbf{L}}}^{-1} + \left( \underline{\mathbf{I}} - \underline{\mathbf{S}}_{\text{Esh}} \right) : \underline{\tilde{\mathbf{C}}}^{-1} \right] : \dot{\boldsymbol{\epsilon}} + \left( \underline{\mathbf{I}} - \underline{\mathbf{S}}_{\text{Esh}} \right) : \left( \dot{\boldsymbol{\epsilon}}_{\text{p}} - \dot{\boldsymbol{\epsilon}}_{\text{p}}^{(r)} \right)$$

Thus, Eq. (A.10) can be rewritten as:

$$\dot{\boldsymbol{\epsilon}}^{(r)} = \underline{\mathbf{a}}_{\text{L}}^{(r-1)} : \left[ \underline{\tilde{\mathbf{a}}}_{\text{L}} : \dot{\boldsymbol{\epsilon}} + \left( \underline{\mathbf{I}} - \underline{\mathbf{S}}_{\text{Esh}} \right) : \left( \dot{\boldsymbol{\epsilon}}_{\text{p}} - \dot{\boldsymbol{\epsilon}}_{\text{p}}^{(r)} \right) \right] \quad (\text{A.14})$$

with the notations

$$\begin{cases} \underline{\mathbf{a}}_{\text{L}}^{(r)} = \underline{\mathbf{S}}_{\text{Esh}} : \underline{\tilde{\mathbf{L}}}^{-1} + \left( \underline{\mathbf{I}} - \underline{\mathbf{S}}_{\text{Esh}} \right) : \underline{\tilde{\mathbf{C}}}^{(r-1)}, \\ \underline{\tilde{\mathbf{a}}}_{\text{L}} = \underline{\mathbf{S}}_{\text{Esh}} : \underline{\tilde{\mathbf{L}}}^{-1} + \left( \underline{\mathbf{I}} - \underline{\mathbf{S}}_{\text{Esh}} \right) : \underline{\tilde{\mathbf{C}}}^{-1}. \end{cases} \quad (\text{A.15})$$

### Appendix A.3. Kröner's assumption

In Kröner (1961),  $\boldsymbol{\epsilon}_{\text{p}}$  was treated as an eigenstrain, and the accommodation by the matrix surrounding the inclusion was assumed to be purely elastic. In this formulation,  $\underline{\mathbf{L}}^*$  in Eq. (A.10) was replaced by  $\underline{\tilde{\mathbf{C}}}: \left( \underline{\mathbf{S}}_{\text{Esh}}^{-1} - \underline{\mathbf{I}} \right)$ , where  $\underline{\mathbf{S}}_{\text{Esh}}$  is calculated with respect to the elastic stiffness tensor  $\underline{\tilde{\mathbf{C}}}$  instead of the tangent elastoplastic moduli  $\underline{\tilde{\mathbf{L}}}$ . Kröner's assumption is used here to simplify Hill's elasto-plastic homogenization model. Thus  $\underline{\mathbf{a}}_{\text{L}}^{(r)}$  and  $\underline{\tilde{\mathbf{a}}}_{\text{L}}$  in Eq. (A.15) become:

$$\begin{cases} \underline{\mathbf{a}}_{\text{L}}^{(r)} = \underline{\mathbf{S}}_{\text{Esh}} : \underline{\tilde{\mathbf{C}}}^{-1} + \left( \underline{\mathbf{I}} - \underline{\mathbf{S}}_{\text{Esh}} \right) : \underline{\mathbf{C}}^{(r-1)}, \\ \underline{\tilde{\mathbf{a}}}_{\text{L}} = \underline{\tilde{\mathbf{C}}}^{-1}. \end{cases} \quad (\text{A.16})$$

Substituting Eq. (A.16) into Eq. (A.14):

$$\dot{\boldsymbol{\epsilon}}^{(r)} = \underline{\mathbf{B}}^{(r)} : \left[ \dot{\boldsymbol{\epsilon}} + \underline{\mathbf{L}}_{\text{C}}^* : \left( \dot{\boldsymbol{\epsilon}}_{\text{p}} - \dot{\boldsymbol{\epsilon}}_{\text{p}}^{(r)} \right) \right] \quad (\text{A.17})$$

where  $\underline{\mathbf{B}}^{(r)}$  is the stress concentration tensor of elastic problems (determined in Eq. (A.4)) and the tensor  $\underline{\mathbf{L}}_{\text{C}}^*$  is expressed as follows:

$$\underline{\mathbf{L}}_{\text{C}}^* = \underline{\tilde{\mathbf{C}}}: \left( \underline{\mathbf{I}} - \underline{\mathbf{S}}_{\text{Esh}} \right) = \underline{\mathbf{C}}^* : \underline{\mathbf{S}}_{\text{Esh}}. \quad (\text{A.18})$$

Moreover, the computations of the Eshelby tensor  $\underline{\mathbf{S}}_{\text{Esh}}$  will receive further attention in Appendix A.4 for both Kröner's elasto-plastic homogenization model (Kröner, 1961) and the  $\beta$ -model.

The interaction equation Eq. (A.17) is purely elastic following Kröner's assumption. The latter has been shown to result in a too stiff overall response and the internal stresses are significantly overestimated (Berveiller and Zaoui, 1978; Masson and Zaoui, 1999). Compared with Hill's model of Appendix A.2, the nonlinearity of the operator multiplying the difference between global and local plastic strain tensors is not taken into account. Nevertheless, this assumption can be taken as a new starting point for an alternative approach, i.e. the  $\beta$ -models, where the nonlinearity is transferred to the term that represents the heterogeneity of plastic strain.

### Appendix A.4. Formulation of $\beta$ -models

#### Appendix A.4.1. General $\beta$ -model

According to (Cailletaud, 1992; Forest and Pilvin, 1996; Sai et al., 2006; Besson et al., 2009; Martin et al., 2014; Cailletaud and Coudon, 2016; Coudon et al., 2018), the heuristic  $\beta$ -models introduce interphase accommodation variables  $\boldsymbol{\beta}^{(r)}$  to replace the local plastic strain  $\boldsymbol{\epsilon}_{\text{p}}^{(r)}$  in Eq. (A.17). Under small-strain conditions, i.e. with negligible microstructure evolution,  $\underline{\mathbf{B}}^{(r)}$  and  $\underline{\mathbf{L}}_{\text{C}}^*$  can be considered as constant. After time integration of Eq. (A.17), the scale transition interaction equation of the  $\beta$ -model is obtained:

$$\boldsymbol{\sigma}^{(r)} = \underset{\approx}{\mathbf{B}}^{(r)} : \left[ \bar{\boldsymbol{\sigma}} + \underset{\approx}{\mathbf{L}}_C^* : (\tilde{\boldsymbol{\beta}} - \boldsymbol{\beta}^{(r)}) \right] + \boldsymbol{\sigma}_{\text{res}}^{(r)}, \quad (\text{A.19})$$

which accounts for both elastic and plastic local heterogeneity. In this relation, the tensors  $\underset{\approx}{\mathbf{B}}^{(r)}$ ,  $\underset{\approx}{\mathbf{L}}_C^*$  and  $\boldsymbol{\sigma}_{\text{res}}^{(r)}$  are still given by Eqs. (A.4), (A.18) and (A.6) respectively. In Eq. (A.19),  $\boldsymbol{\sigma}^{(r)}$  is initialized as  $\boldsymbol{\sigma}_{\text{res}}^{(r)}$  before loading. In a similar way as for plastic strain  $\boldsymbol{\varepsilon}_p^{(r)}$ , the  $\boldsymbol{\beta}^{(r)}$  variables are also initialized at  $\mathbf{0}$ . In the elastic regime, Eq. (A.19) reduces to Eq. (A.3).

Furthermore, it should be noticed that in the  $\beta$  and Kröner's elasto-plastic models,  $\underset{\approx}{\mathbf{S}}_{\text{Esh}}$  is computed by using  $\tilde{\underset{\approx}{\mathbf{C}}}$  instead of  $\tilde{\underset{\approx}{\mathbf{L}}}$  as in Hill's approach. In this way, considerable CPU time can be saved since  $\underset{\approx}{\mathbf{S}}_{\text{Esh}}$  is evaluated only once. In contrast, Hill's model Appendix (A.2) requires the computation of  $\underset{\approx}{\mathbf{S}}_{\text{Esh}}$  at each loading step due to the evolution of  $\tilde{\underset{\approx}{\mathbf{L}}}$  along the deformation path.

Inspired by the kinematic hardening evolution rule in Lemaitre and Chaboche (1994), a time-independent non-linear evolution equation for the  $\beta$ -variables is used:

$$\dot{\boldsymbol{\beta}}^{(r)} = \dot{\boldsymbol{\varepsilon}}_p^{(r)} - \underset{\approx}{\mathbf{D}} : \boldsymbol{\beta}^{(r)} \|\dot{\boldsymbol{\varepsilon}}_p^{(r)}\| \quad (\text{A.20})$$

where the plastic strain rate is the driving force and the tensor  $\underset{\approx}{\mathbf{D}}$  denotes a constant phenomenological tensor whose components must be calibrated in order to correct the approximation introduced for  $\underset{\approx}{\mathbf{S}}_{\text{Esh}}$ . The form of  $\underset{\approx}{\mathbf{D}}$  and its identification are presented and discussed in Sections 3.3 and 4.3 respectively.

$$\|\dot{\boldsymbol{\varepsilon}}_p^{(r)}\| = \sqrt{\frac{2}{3} (\dot{\boldsymbol{\varepsilon}}_p^{(r)})_{ij} (\dot{\boldsymbol{\varepsilon}}_p^{(r)})_{ij}}. \quad (\text{A.21})$$

Finally, the homogenization condition  $\bar{\boldsymbol{\sigma}} = \langle \boldsymbol{\sigma}^{(r)} \rangle$  is used to determine the effective accommodation variable  $\tilde{\boldsymbol{\beta}}$  after combining Eq. (A.19) and (A.5) and accounting for  $\langle \boldsymbol{\sigma}_{\text{res}}^{(r)} \rangle = \mathbf{0}$ :

$$\tilde{\boldsymbol{\beta}} = \langle \underset{\approx}{\mathbf{L}}_C^{*-1} : \underset{\approx}{\mathbf{B}}^{(r)} : \underset{\approx}{\mathbf{L}}_C^* : \boldsymbol{\beta}^{(r)} \rangle. \quad (\text{A.22})$$

The macroscopic plastic strain response  $\tilde{\boldsymbol{\varepsilon}}_p$  can be computed by substituting Eqs. (A.11) and (A.12) into Eq. (A.19):

$$\begin{aligned} \underset{\approx}{\mathbf{C}}^{(r)} \left( \boldsymbol{\varepsilon}^{(r)} - \boldsymbol{\varepsilon}_p^{(r)} - \boldsymbol{\varepsilon}_0^{(r)} \right) &= \underset{\approx}{\mathbf{B}}^{(r)} : \tilde{\underset{\approx}{\mathbf{C}}} (\bar{\boldsymbol{\varepsilon}} - \tilde{\boldsymbol{\varepsilon}}_p - \tilde{\boldsymbol{\varepsilon}}_0) + \underset{\approx}{\mathbf{B}}^{(r)} : \underset{\approx}{\mathbf{L}}_C^* : (\tilde{\boldsymbol{\beta}} - \boldsymbol{\beta}^{(r)}) + \boldsymbol{\sigma}_{\text{res}}^{(r)} \\ \Leftrightarrow \\ \left( \underset{\approx}{\mathbf{C}}^{(r)-1} : \underset{\approx}{\mathbf{B}}^{(r)} : \tilde{\underset{\approx}{\mathbf{C}}} \right) : \tilde{\boldsymbol{\varepsilon}}_p &= \boldsymbol{\varepsilon}_p^{(r)} - \boldsymbol{\varepsilon}^{(r)} + \boldsymbol{\varepsilon}_0^{(r)} + \left( \underset{\approx}{\mathbf{C}}^{(r)-1} : \underset{\approx}{\mathbf{B}}^{(r)} : \tilde{\underset{\approx}{\mathbf{C}}} \right) : \bar{\boldsymbol{\varepsilon}} \\ &- \left( \underset{\approx}{\mathbf{C}}^{(r)-1} : \underset{\approx}{\mathbf{B}}^{(r)} : \tilde{\underset{\approx}{\mathbf{C}}} \right) : \tilde{\boldsymbol{\varepsilon}}_0 + \underset{\approx}{\mathbf{C}}^{(r)-1} : \underset{\approx}{\mathbf{B}}^{(r)} : \underset{\approx}{\mathbf{L}}_C^* : (\tilde{\boldsymbol{\beta}} - \boldsymbol{\beta}^{(r)}) + \underset{\approx}{\mathbf{C}}^{(r)-1} : \boldsymbol{\sigma}_{\text{res}}^{(r)} \\ \Leftrightarrow \\ \langle \underset{\approx}{\mathbf{C}}^{(r)-1} : \underset{\approx}{\mathbf{B}}^{(r)} : \tilde{\underset{\approx}{\mathbf{C}}} \rangle : \tilde{\boldsymbol{\varepsilon}}_p &= \tilde{\boldsymbol{\varepsilon}}_p - \bar{\boldsymbol{\varepsilon}} + \langle \boldsymbol{\varepsilon}_0^{(r)} \rangle + \langle \underset{\approx}{\mathbf{C}}^{(r)-1} : \underset{\approx}{\mathbf{B}}^{(r)} : \tilde{\underset{\approx}{\mathbf{C}}} \rangle : \bar{\boldsymbol{\varepsilon}} \\ &- \langle \underset{\approx}{\mathbf{C}}^{(r)-1} : \underset{\approx}{\mathbf{B}}^{(r)} : \tilde{\underset{\approx}{\mathbf{C}}} \rangle : \tilde{\boldsymbol{\varepsilon}}_0 + \langle \underset{\approx}{\mathbf{C}}^{(r)-1} : \underset{\approx}{\mathbf{B}}^{(r)} : \underset{\approx}{\mathbf{L}}_C^* : (\tilde{\boldsymbol{\beta}} - \boldsymbol{\beta}^{(r)}) \rangle + \langle \underset{\approx}{\mathbf{C}}^{(r)-1} : \boldsymbol{\sigma}_{\text{res}}^{(r)} \rangle \end{aligned}$$

The following two relations are derived from Eq. (A.2) and Eq. (A.8):

$$\langle \underset{\approx}{\mathbf{C}}^{(r)-1} : \underset{\approx}{\mathbf{B}}^{(r)} : \tilde{\underset{\approx}{\mathbf{C}}} \rangle = \underset{\approx}{\mathbf{I}}, \quad \tilde{\boldsymbol{\varepsilon}}_0 = \langle \boldsymbol{\varepsilon}_0^{(r)} \rangle + \langle \underset{\approx}{\mathbf{C}}^{(r)-1} : \boldsymbol{\sigma}_{\text{res}}^{(r)} \rangle.$$

The second equation provides the macroscopic eigenstrain as a function of local eigenstrains and residual stresses. Finally, the expression of the macroscopic plastic strain  $\tilde{\boldsymbol{\varepsilon}}_p$  can be reduced to:

$$\tilde{\boldsymbol{\varepsilon}}_p = \bar{\boldsymbol{\varepsilon}}_p + \langle \underset{\approx}{\mathbf{C}}^{(r)-1} : \underset{\approx}{\mathbf{B}}^{(r)} : \underset{\approx}{\mathbf{L}}_C^* : (\tilde{\boldsymbol{\beta}} - \boldsymbol{\beta}^{(r)}) \rangle. \quad (\text{A.23})$$

#### Appendix A.4.2. $\beta$ -model with homogeneous local elastic behavior

The previous general formulation represents in fact a new extension of the  $\beta$ -model taking into account the heterogeneous local elasticity (Ausias et al., 2007; Cailletaud and Coudon, 2016; Coudon et al., 2018) and initial residual stresses  $\boldsymbol{\sigma}_{\text{res}}^{(r)}$ . In the present section, the earlier versions of  $\beta$ -models, e.g. (Sai et al., 2006; Martin et al., 2014), are derived from the previous general formulation in the particular case of homogeneous elastic behavior. According to the earlier versions, it is assumed that the main source of mechanical heterogeneity is plasticity more than elasticity (Cailletaud, 1992; Besson et al., 2009). In other words, the polycrystalline aggregate exhibit a homogeneous local elastic behavior:  $\underset{\approx}{\mathbf{C}}^{(r)} = \underset{\approx}{\mathbf{C}} = \tilde{\underset{\approx}{\mathbf{C}}}$ . The stress concentration tensor  $\underset{\approx}{\mathbf{B}}^{(r)}$  in Eq. (A.4) becomes the identity  $\underset{\approx}{\mathbf{I}}$ , and  $\tilde{\boldsymbol{\beta}}$  reduces to the average  $\langle \boldsymbol{\beta}^{(r)} \rangle = \bar{\boldsymbol{\beta}}$ . Therefore, Eq. (A.19) can be simplified as follows (assuming here  $\boldsymbol{\sigma}_{\text{res}}^{(r)} = \mathbf{0}$ ):

$$\boldsymbol{\sigma}^{(r)} = \bar{\boldsymbol{\sigma}} + \underset{\approx}{\mathbf{L}}_C^* : \left( \bar{\boldsymbol{\beta}} - \boldsymbol{\beta}^{(r)} \right) \quad (\text{A.24})$$

where  $\underset{\approx}{\mathbf{L}}_C^*$  and  $\boldsymbol{\beta}^{(r)}$  are still given by Eq. (A.18) and (A.20) respectively.

In particular, if the phenomenological tensor  $\underline{\underline{D}}$  in Eq. (A.20) vanishes, we get  $\underline{\underline{\beta}}^{(r)} = \underline{\underline{\varepsilon}}_p^{(r)}$  and therefore  $\underline{\underline{\beta}} = \underline{\underline{\varepsilon}}_p$ . In this case, the  $\beta$ -model reduces to Kröner's elasto-plastic homogenization model (Kröner, 1961):

$$\underline{\underline{\sigma}}^{(r)} = \underline{\underline{\sigma}} + \underline{\underline{L}}_C^* : \left( \underline{\underline{\varepsilon}}_p - \underline{\underline{\varepsilon}}_p^{(r)} \right). \quad (\text{A.25})$$

## References

- Asaro, R.J., 1983. In: *Micromechanics of Crystals and Polycrystals*, vol 23. Elsevier, pp. 1–115 of *Advances in Applied Mechanics*.
- Ausias, G., Thuillier, S., Omnes, B., Wiessner, S., Pilvin, P., 2007. Micro-mechanical model of TPE made of polypropylene and rubber waste. *Polymer* 48, 3367–3376.
- Badinier, G., Sinclair, C., Allain, S., Bouaziz, O., 2014. The Bauschinger effect in drawn and annealed nanocomposite Cu–Nb wires. *Mater. Sci. Eng. A* 597, 10–19.
- Barbe, F., Decker, L., Jeulin, D., Cailletaud, G., 2001a. Intergranular and intragranular behavior of polycrystalline aggregates. Part 1: FE model. *Int. J. Plast.* 17, 513–536.
- Barbe, F., Forest, S., Cailletaud, G., 2001b. Intergranular and intragranular behavior of polycrystalline aggregates. Part 2: Results. *Int. J. Plast.* 17, 537–563.
- Béard, J., Billette, J., Frings, P., Suleiman, M., Lecouturier, F., 2013. Special coils development at the national high magnetic field laboratory in Toulouse. *J. Low Temp. Phys.* 170, 442–446.
- Béard, J., Billette, J., Ferreira, N., Frings, P., Lagarrigue, J.M., Lecouturier, F., Nicolin, J.P., 2018. Design and tests of the 100-T triple coil at LNCMI. *IEEE Trans. Appl. Supercond.* 28, 1–5.
- Berveiller, M., Zaoui, A., 1978. An extension of the self-consistent scheme to plastically-flowing polycrystals. *J. Mech. Phys. Solids* 26, 325–344.
- Besson, J., Cailletaud, G., Chaboche, J., Forest, S., 2009. In: *Non-linear Mechanics of Materials*, vol 167 Springer.
- Beyerlein, I.J., Mayeur, J.R., Zheng, S., Mara, N.A., Wang, J., Misra, A., 2014. Emergence of stable interfaces under extreme plastic deformation. *Proc. Natl. Acad. Sci. Unit. States Am.* 111, 4386–4390.
- Brenner, R., Masson, R., Castelnau, O., Zaoui, A., 2002. A quasi-elastic affine formulation for the homogenised behaviour of nonlinear viscoelastic polycrystals and composites. *Eur. J. Mech. A Solid.* 21, 943–960.
- Brenner, R., Castelnau, O., Badae, L., 2004. Mechanical field fluctuations in polycrystals estimated by homogenization techniques. *Proc. R. Soc. London, Ser. A: Math. Phys. Eng. Sci.* 460, 3589–3612.
- Cailletaud, G., 1992. A micromechanical approach to inelastic behaviour of metals. *Int. J. Plast.* 8, 55–73.
- Cailletaud, G., Coudon, F., 2016. Scale transition rules applied to crystal plasticity. In: *Materials with Internal Structure*. Springer, pp. 1–15.
- Castañeda, P.P., 1991. The effective mechanical properties of nonlinear isotropic composites. *J. Mech. Phys. Solids* 39, 45–71.
- Castañeda, P.P., 2002. Second-order homogenization estimates for nonlinear composites incorporating field fluctuations: I theory. *J. Mech. Phys. Solids* 50, 737–757.
- Castelnau, O., 2011. Mechanical behavior of polycrystalline materials. In: Thomas, O., Ponchet, A., Forest, S. (Eds.), *Mechanics of Nano-Objects*. Presses des MINES, Paris, pp. 301–322 (chapter 5).
- Choi, H.J., McDowell, D.L., Allen, J.K., Mistree, F., 2008. An inductive design exploration method for hierarchical systems design under uncertainty. *Eng. Optim.* 40, 287–307.
- Coudon, F., 2017. *Mechanical Behavior of the Directionally Solidified Nickel-Base Superalloy DS200 + Hf*. Ph.D. Thesis. MINES ParisTech. PSL Research University.
- Coudon, F., Cailletaud, G., Cormier, J., Marcin, L., 2018. A multiscale model for nickel-based directionally solidified materials. *Int. J. Plast.* 115, 1–17. <https://doi.org/10.1016/j.ijplas.2018.10.003>.
- Debray, F., Frings, P., 2013. State of the art and developments of high field magnets at the Laboratoire National des Champs Magnétiques Intenses. *Compt. Rendus Phys.* 14, 2–14.
- Devincere, B., Hoc, T., Kubin, L., 2008. Dislocation mean free paths and strain hardening of crystals. *Science* 320, 1745–1748.
- Doghri, I., Brassart, L., Adam, L., Gérard, J.S., 2011. A second-moment incremental formulation for the mean-field homogenization of elasto-plastic composites. *Int. J. Plast.* 27, 352–371.
- Dubois, J., 2010. *Conducteurs nanocomposites métalliques élaborés par déformation plastique sévère : formation et stabilité thermo-mécanique des nanostructures, propriétés induites*. Ph.D. thesis. Université de Poitiers.
- Dubois, J., Thilly, L., Renault, P., Lecouturier, F., Di Michiel, M., 2010. Thermal stability of nanocomposite metals: in situ observation of anomalous residual stress relaxation during annealing under synchrotron radiation. *Acta Mater.* 58, 6504–6512.
- Dubois, J., Thilly, L., Lecouturier, F., Olier, P., Renault, P., 2012. Cu/Nb nanocomposite wires processed by severe plastic deformation for applications in high pulsed magnets: effects of the multi-scale microstructure on the mechanical properties. *IEEE Trans. Appl. Supercond.* 22, 6900104.
- Dupouy, F., Askenazy, S., Peyrade, J., Legat, D., 1995. Composite conductors for high pulsed magnetic fields. *Phys. B Condens. Matter* 211, 43–45.
- Dupouy, F., Snoeck, E., Casanove, M., Roucau, C., Peyrade, J., Askenazy, S., 1996. Microstructural characterization of high strength and high conductivity nanocomposite wires. *Scripta Mater.* 34, 1067–1073.
- Eshelby, J.D., 1957. The determination of the elastic field of an ellipsoidal inclusion, and related problems. In: *Proceedings of the Royal Society of London A: Mathematical, Physical and Engineering Sciences*. The Royal Society, pp. 376–396.
- Feyel, F., Chaboche, J.L., 2000. FE2 multiscale approach for modelling the elastoviscoplastic behaviour of long fibre SiC/Ti composite materials. *Comput. Methods Appl. Mech. Eng.* 183, 309–330.
- Forest, S., Pilvin, P., 1996. Modelling the cyclic behaviour of two-phase single crystal nickel-base superalloys. In: *IUTAM Symposium on Micromechanics of Plasticity and Damage of Multiphase Materials*. Springer, pp. 51–58.
- Franciosi, P., Berbenni, S., 2008. Multi-laminate plastic-strain organization for non-uniform tfa modeling of poly-crystal regularized plastic flow. *Int. J. Plast.* 24, 1549–1580.
- François, D., Pineau, A., Zaoui, A., 1998. *Mechanical Behaviour of Materials*. Springer.
- Fritzen, F., Böhlke, T., 2011. Nonuniform transformation field analysis of materials with morphological anisotropy. *Compos. Sci. Technol.* 71, 433–442.
- Frydman, L., 2014. High magnetic field science and its application in the United States: a magnetic resonance perspective. *J. Magn. Reson.* 242, 256–264.
- Geers, M.G., Kouznetsova, V.G., Brekelmans, W., 2010. Multi-scale computational homogenization: trends and challenges. *J. Comput. Appl. Math.* 234, 2175–2182.
- Gérard, C., 2008. *Mesures de champs et identification de modèles de plasticité cristalline*. Ph.D. thesis. Université Paris-Nord-Paris XIII.
- Gérard, C., Cailletaud, G., Bacroix, B., 2013. Modeling of latent hardening produced by complex loading paths in FCC alloys. *Int. J. Plast.* 42, 194–212.
- Groh, S., Marin, E., Horstemeyer, M., Zbib, H., 2009. Multiscale modeling of the plasticity in an aluminum single crystal. *Int. J. Plast.* 25, 1456–1473.
- Gu, T., Hervé-Luanco, E., Proudhon, H., Thilly, L., Dubois, J.B., Lecouturier, F., Castelnau, O., Forest, S., 2015. Modélisation multi-échelle du comportement électrique de nano-composites Cu-Nb. *Matériaux Tech.* 103, 309.
- Gu, T., Castelnau, O., Forest, S., Hervé-Luanco, E., Lecouturier, F., Proudhon, H., Thilly, L., 2017a. Multiscale modeling of the elastic behavior of architected and nanostructured Cu-Nb composite wires. *Int. J. Solids Struct.*
- Gu, T., Medy, J.R., Volpi, F., Castelnau, O., Forest, S., Hervé-Luanco, E., Lecouturier, F., Proudhon, H., Renault, P.O., Thilly, L., 2017b. Multiscale modeling of the anisotropic electrical conductivity of architected and nanostructured Cu-Nb composite wires and experimental comparison. *Acta Mater.*
- Haddadi, H., Bouvier, S., Banu, M., Maier, C., Teodosiu, C., 2006. Towards an accurate description of the anisotropic behaviour of sheet metals under large plastic deformations: modelling, numerical analysis and identification. *Int. J. Plast.* 22, 2226–2271.
- Halperin, B., Aepli, G., Ando, Y., Aronson, M., Basov, D., Budinger, T., Dimeo, R., Gore, J., Hunte, F., Lau, C., et al., 2013. *High Magnetic Field Science and its*

- Application in the united states: Current Status and Future Directions. National Academy of Sciences, Washington, DC.
- Hansen, B., Carpenter, J., Sintay, S., Bronkhorst, C., McCabe, R., Mayeur, J., Mourad, H., Beyerlein, I., Mara, N., Chen, S., et al., 2013. Modeling the texture evolution of cu/nb layered composites during rolling. *Int. J. Plast.* 49, 71–84.
- Hill, R., 1965. Continuum micro-mechanics of elastoplastic polycrystals. *J. Mech. Phys. Solids* 13, 89–101.
- Hoc, T., Forest, S., 2001. Polycrystal modelling of IF-Ti steel under complex loading path. *Int. J. Plast.* 17, 65–85.
- Hutchinson, J., 1976. Bounds and self-consistent estimates for creep of polycrystalline materials. In: *Proceedings of the Royal Society of London A: Mathematical, Physical and Engineering Sciences*. The Royal Society, pp. 101–127.
- Idiart, M., Moulinec, H., Castañeda, P.P., Suquet, P., 2006. Macroscopic behavior and field fluctuations in viscoplastic composites: second-order estimates versus full-field simulations. *J. Mech. Phys. Solids* 54, 1029–1063.
- Jaime, M., Daou, R., Crooker, S.A., Weickert, F., Uchida, A., Feiguin, A.E., Batista, C.D., Dabkowska, H.A., Gaulin, B.D., 2012. Magnetostriction and magnetic texture to 100.75 Tesla in frustrated SrCu<sub>2</sub>(BO<sub>3</sub>)<sub>2</sub>. *Proc. Natl. Acad. Sci. Unit. States Am.* 109, 12404–12407.
- Kanit, T., Forest, S., Galliet, I., Mounoury, V., Jeulin, D., 2003. Determination of the size of the representative volume element for random composites: statistical and numerical approach. *Int. J. Solids Struct.* 40, 3647–3679.
- Kröner, E., 1961. On the plastic deformation of polycrystals. *Acta Metall.* 9, 155–161.
- Kröner, E., 1978. Self-consistent scheme and graded disorder in polycrystal elasticity. *J. Phys. F Met. Phys.* 8, 2261.
- Kubin, L., Devincere, B., Hoc, T., 2008. Modeling dislocation storage rates and mean free paths in face-centered cubic crystals. *Acta Mater.* 56, 6040–6049.
- Lebensohn, R., Tomé, C., 1994. A self-consistent viscoplastic model: prediction of rolling textures of anisotropic polycrystals. *Mater. Sci. Eng. A* 175, 71–82.
- Lebensohn, R.A., Kanjarla, A.K., Eisenlohr, P., 2012. An elasto-viscoplastic formulation based on fast fourier transforms for the prediction of micromechanical fields in polycrystalline materials. *Int. J. Plast.* 32, 59–69.
- Lee, S.B., LeDonne, J., Lim, S., Beyerlein, I., Rollett, A., 2012. The heterophase interface character distribution of physical vapor-deposited and accumulative roll-bonded cu–nb multilayer composites. *Acta Mater.* 60, 1747–1761.
- Lemaitre, J., Chaboche, J.L., 1994. *Mechanics of Solid Materials*. Cambridge university press.
- Lim, S., Rollett, A., 2009. Length scale effects on recrystallization and texture evolution in cu layers of a roll-bonded cu–nb composite. *Mater. Sci. Eng. A* 520, 189–196.
- Lu, L., Li, S., Lu, K., 2001. An abnormal strain rate effect on tensile behavior in nanocrystalline copper. *Scripta Mater.* 45, 1163–1169.
- Martin, G., Ochoa, N., Sai, K., Hervé-Luanco, E., Cailletaud, G., 2014. A multiscale model for the elastoviscoplastic behavior of directionally solidified alloys: application to FE structural computations. *Int. J. Solids Struct.* 51, 1175–1187.
- Masson, R., Zaoui, A., 1999. Self-consistent estimates for the rate-dependent elastoplastic behaviour of polycrystalline materials. *J. Mech. Phys. Solids* 47, 1543–1568.
- Masson, R., Bornert, M., Suquet, P., Zaoui, A., 2000. An affine formulation for the prediction of the effective properties of nonlinear composites and polycrystals. *J. Mech. Phys. Solids* 48, 1203–1227.
- Mayeur, J., Beyerlein, I., Bronkhorst, C., Mourad, H., Hansen, B., 2013. A crystal plasticity study of heterophase interface character stability of cu/nb bicrystals. *Int. J. Plast.* 48, 72–91.
- Mayeur, J., Beyerlein, I., Bronkhorst, C., Mourad, H., 2015. Incorporating interface affected zones into crystal plasticity. *Int. J. Plast.* 65, 206–225.
- McDowell, D.L., 2010. A perspective on trends in multiscale plasticity. *Int. J. Plast.* 26, 1280–1309.
- Medy, J.R., 2016. Evaluation des effets de taille et d'architecture sur les propriétés mécaniques et électriques de fils composites métalliques cuivre/niobium fabriqués par déformation plastique sévère. Ph.D. thesis. Université de Poitiers.
- Méric, L., Poubanne, P., Cailletaud, G., 1991. Single crystal modeling for structural calculations: part 1—model presentation. *J. Eng. Mater. Technol.* 113, 162–170.
- Méric, L., Cailletaud, G., Gaspérini, M., 1994. FE calculations of copper bicrystal specimens submitted to tension-compression tests. *Acta Metall. Mater.* 42, 921–935.
- Meyers, M.A., Andrade, U.R., Chokshi, A.H., 1995. The effect of grain size on the high-strain, high-strain-rate behavior of copper. *Metall. Mater. Trans. A* 26, 2881–2893.
- Michel, J.C., Suquet, P., 2003. Nonuniform transformation field analysis. *Int. J. Solids Struct.* 40, 6937–6955.
- Michel, J.C., Suquet, P., 2004. Computational analysis of nonlinear composite structures using the nonuniform transformation field analysis. *Comput. Methods Appl. Mech. Eng.* 193, 5477–5502.
- Michel, J.C., Suquet, P., 2016. A model-reduction approach in micromechanics of materials preserving the variational structure of constitutive relations. *J. Mech. Phys. Solids* 90, 254–285.
- Misra, A., Hoagland, R., 2007. Plastic flow stability of metallic nanolaminate composites. *J. Mater. Sci.* 42, 1765–1771.
- Misra, A., Thilly, L., 2010. Structural metals at extremes. *MRS Bull.* 35, 965–976.
- Molinari, A., Canova, G., Ahzi, S., 1987. A self consistent approach of the large deformation polycrystal viscoplasticity. *Acta Metall.* 35, 2983–2994.
- Moulinec, H., Suquet, P., 1995. A FFT-based numerical method for computing the mechanical properties of composites from images of their microstructures. In: *IUTAM Symposium on Microstructure-Property Interactions in Composite Materials*. Springer, pp. 235–246.
- Mura, T., 1987. *Micromechanics of Defects in Solids*. Springer Science & Business Media.
- Musienko, A., Tatschl, A., Schmidegg, K., Kolednik, O., Pippan, R., Cailletaud, G., 2007. Three-dimensional finite element simulation of a polycrystalline copper specimen. *Acta Mater.* 55, 4121–4136.
- Neil, C., Wollmershauser, J., Clausen, B., Tomé, C., Agnew, S., 2010. Modeling lattice strain evolution at finite strains and experimental verification for copper and stainless steel using in situ neutron diffraction. *Int. J. Plast.* 26, 1772–1791.
- Nemat-Nasser, S., Hori, M., 2013. *Micromechanics: Overall Properties of Heterogeneous Materials*. Elsevier.
- Nguyen, D.N., Michel, J., Mielke, C.H., 2016. Status and development of pulsed magnets at the NHMFL pulsed field facility. *IEEE Trans. Appl. Supercond.* 26, 1–5.
- Nizolek, T., Mara, N.A., Beyerlein, L.J., Avallone, J.T., Pollock, T.M., 2015. Enhanced plasticity via kinking in cubic metallic nanolaminates. *Adv. Eng. Mater.* 17, 781–785.
- Pan, B., Qian, K., Xie, H., Asundi, A., 2009. Two-dimensional digital image correlation for in-plane displacement and strain measurement: a review. *Meas. Sci. Technol.* 20, 062001.
- Paquin, A., Sabar, H., Berveiller, M., 1999. Integral formulation and self-consistent modelling of elastoviscoplastic behavior of heterogeneous materials. *Arch. Appl. Mech.* 69, 14–35.
- Paquin, A., Berbenni, S., Favier, V., Lemoine, X., Berveiller, M., 2001. Micromechanical modeling of the elastic–viscoplastic behavior of polycrystalline steels. *Int. J. Plast.* 17, 1267–1302.
- Peng, T., Jiang, F., Sun, Q., Xu, Q., Xiao, H., Herlach, F., Li, L., 2014. Design and test of a 90-Tx nondestructive magnet at the wuhan national high magnetic field center. *IEEE Trans. Appl. Supercond.* 24, 1–4.
- Pilvin, P., 1996. The contribution of micromechanical approaches to the modelling of inelastic behaviour of polycrystals. In: Pineau, A., Cailletaud, G., Lindley, T. (Eds.), *Fourth Int. Conf. On Biaxial/multiaxial Fatigue and Design*, ESIS 21. Mechanical Engineering Publications, London, pp. 3–19.
- Ponte-Castañeda, P., Suquet, P., 1998. Nonlinear composites. *Adv. Appl. Mech.* 34, 171–302.
- Prakash, A., Lebensohn, R., 2009. Simulation of micromechanical behavior of polycrystals: finite elements versus fast fourier transforms. *Model. Simul. Mater. Sci. Eng.* 17, 064010.
- Qu, J., Cherkaoui, M., 2006. *Fundamentals of Micromechanics of Solids*. Wiley, Hoboken.
- Sai, K., Cailletaud, G., Forest, S., 2006. Micro-mechanical modeling of the inelastic behavior of directionally solidified materials. *Mech. Mater.* 38, 203–217.
- Šiška, F., Forest, S., Gumbsch, P., Weygand, D., 2006. Finite element simulations of the cyclic elastoplastic behaviour of copper thin films. *Model. Simul. Mater. Sci. Eng.* 15, S217.
- Šiška, F., Weygand, D., Forest, S., Gumbsch, P., 2009. Comparison of mechanical behaviour of thin film simulated by discrete dislocation dynamics and continuum crystal plasticity. *Comput. Mater. Sci.* 45, 793–799.
- Spencer, K., Lecouturier, F., Thilly, L., Embury, J., 2004. Established and emerging materials for use as high-field magnet conductors. *Adv. Eng. Mater.* 6, 290–297.
- Suquet, P., Moulinec, H., Castelnaud, O., Montagnat, M., Lahellec, N., Grennerat, F., Duval, P., Brenner, R., 2012. Multi-scale modeling of the mechanical behavior of

- polycrystalline ice under transient creep. *Procedia IUTAM* 3, 76–90.
- Suvorov, A.P., Dvorak, G.J., 2002. Rate form of the Eshelby and Hill tensors. *Int. J. Solids Struct.* 39, 5659–5678.
- Tabourot, L., Fivel, M., Rauch, E., 1997. Generalised constitutive laws for f.c.c. single crystals. *Mater. Sci. Eng. A* 234, 639–642.
- Thilly, L., 2000. Exploration théorique et expérimentale de fils nanocomposites continus présentant des propriétés extrêmes de conductivité électrique et de limite élastique. Ph.D. thesis. Institut National des Sciences Appliquées de Toulouse.
- Thilly, L., Veron, M., Ludwig, O., Lecouturier, F., 2001. Deformation mechanism in high strength Cu/Nb nanocomposites. *Mater. Sci. Eng. A* 309, 510–513.
- Thilly, L., Lecouturier, F., Von Stebut, J., 2002. Size-induced enhanced mechanical properties of nanocomposite copper/niobium wires: nanoindentation study. *Acta Mater.* 50, 5049–5065.
- Thilly, L., Renault, P., Van Petegem, S., Brandstetter, S., Schmitt, B., Van Swygenhoven, H., Vidal, V., Lecouturier, F., 2007. Evidence of internal Bauschinger test in nanocomposite wires during in situ macroscopic tensile cycling under synchrotron beam. *Appl. Phys. Lett.* 90, 241907.
- Thilly, L., Van Petegem, S., Renault, P., Lecouturier, F., Vidal, V., Schmitt, B., Van Swygenhoven, H., 2009. A new criterion for elasto-plastic transition in nano-materials: application to size and composite effects on Cu–Nb nanocomposite wires. *Acta Mater.* 57, 3157–3169.
- Turner, P., Tomé, C., 1994. A study of residual stresses in Zircaloy-2 with rod texture. *Acta Metall. Mater.* 42, 4143–4153.
- Upadhyay, M., Van Petegem, S., Panzner, T., Lebensohn, R., Van Swygenhoven, H., 2016. Study of lattice strain evolution during biaxial deformation of stainless steel using a finite element and Fast Fourier Transform based multi-scale approach. *Acta Mater.* 118, 28–43.
- Vidal, V., 2006. Optimisation des propriétés mécaniques des conducteurs nanofilamentaires Cu/X (X=Nb ou Ta) par l'étude des mécanismes élémentaires de déformation. Ph.D. thesis. Docteur de l'Institut National des Sciences Appliquées de Toulouse.
- Vidal, V., Thilly, L., Lecouturier, F., Renault, P., 2007. Cu nanowhiskers embedded in Nb nanotubes inside a multiscale Cu matrix: the way to reach extreme mechanical properties in high strength conductors. *Scripta Mater.* 57, 245–248.
- Vidal, V., Thilly, L., Van Petegem, S., Stühr, U., Lecouturier, F., Renault, P.O., Van Swygenhoven, H., 2009. Plasticity of nanostructured Cu–Nb-based wires: strengthening mechanisms revealed by in situ deformation under neutrons. *Scripta Mater.* 60, 171–174.
- Vu, Q.H., Brenner, R., Castelnau, O., Moulinec, H., Suquet, P., 2012. A self-consistent estimate for linear viscoelastic polycrystals with internal variables inferred from the collocation method. *Model. Simul. Mater. Sci. Eng.* 20, 024003.
- Williams, T., Pindera, M.J., 1997. An analytical model for the inelastic axial shear response of unidirectional metal matrix composites. *Int. J. Plast.* 13, 261–289.
- Wu, L., Noels, L., Adam, L., Doghri, I., 2013. A combined incremental-secant mean-field homogenization scheme with per-phase residual strains for elasto-plastic composites. *Int. J. Plast.* 51, 80–102.
- Z-set package, 2013. *Non-linear Material & Structure Analysis Suite*. [www.zset-software.com](http://www.zset-software.com).
- Zecevic, M., Knezevic, M., 2015. A dislocation density based elasto-plastic self-consistent model for the prediction of cyclic deformation: application to AA6022-T4. *Int. J. Plast.* 72, 200–217.
- Zherlitsyn, S., Wustmann, B., Herrmannsdörfer, T., Wosnitza, J., 2013. Magnet-technology development at the Dresden high magnetic field laboratory. *J. Low Temp. Phys.* 170, 447–451.